3-D sediment-basement tomography of the Northern Marmara trough by a dense OBS network at the nodes of a grid of controlled source profiles along the North Anatolian fault

G. Bayrakci,[1,2] M. Laigle,[3,2] A. Bécel,[4,2] A. Hirn,[2] T. Taymaz,[5] S. Yolsal-Çevikbilen[5] and SEISMARMARA team

[1] *Laboratoire Géophysique et Géodynamique, Ifremer, France. Email: gaye.bayrakci@ifremer.fr*
[2] *Laboratoire de Sismologie, Institut de Physique du Globe de Paris, France*
[3] *Dynamique des Marges Convergentes, Geoazur - UMR7329, France*
[4] *Division of Marine Geology and Geophysics, Lamont-Doherty Earth Observatory, Palisades, NY 10964, USA*
[5] *Department of Geophysical Engineering, The Faculty of Mines, Istanbul Technical University, Maslak, TR-34469, Istanbul, Turkey*

SUMMARY

A 3-D tomographic inversion of first arrival times of shot profiles recorded by a dense 2-D OBS network provides an unprecedented constraint on the *P*-wave velocities heterogeneity of the upper-crustal part of the North Marmara Trough (NMT), over a region of 180 km long by 50 km wide. One of the specific aims of this controlled source tomography is to provide a 3-D initial model for the local earthquake tomography (LET). Hence, in an original way, the controlled source inversion has been performed by using a code dedicated to LET. After several tests to check the results trade-off with the inversion parameters, we build up a 3-D *a priori* velocity model, in which the sea-bottom topography, the acoustic and the crystalline basements and the Moho interfaces have been considered. The reliability of the obtained features has been checked by checkerboard tests and also by their comparison with the deep-penetration multichannel seismic profiles, and with the wide-angle reflection and refraction modelled profiles. This study provides the first 3-D view of the basement topography along the active North Anatolian fault beneath the Marmara Sea, even beneath the deepest part of three sedimentary basins of NMT. Clear basement depressions reaching down 6 km depth below the sea level (bsl) have been found beneath these basins. The North Imralı Basin located on the southern continental shelf is observed with a similar sedimentary thickness as its northern neighbours. Between Central and Çınarcık basins, the Central High rises up to 3 km depth below (bsl). Its crest position is offset by 10 km northwestward relatively to the bathymetric crest. On the contrary, Tekirdağ and Central basins appear linked, forming a 60-km-long basement depression. Beneath the bathymetric relief of Western High low velocities are observed down to 6 km depth (bsl) and no basement high have been found. The obtained 3-D *Vp* heterogeneity model allows the consideration of the 3-D supracrustal heterogeneity into the future earthquake relocations in this region. The topographic map of the pre-kinematic basement offers the possibility to take into account the locking depth variations in future geohazard estimations by geomechanical modelling in this region.

Key words: Body waves; Seismic tomography; Continental tectonics: strike-slip and transform; Crustal structure.

1 INTRODUCTION

1.1 Geodynamical setting

The North Anatolian fault (NAF) forms the continental transform boundary between the Eurasian and Anatolian plates (Fig. 1). It extends over more than 1500 km and it is accommodating about 25 mm yr^{-1} (McClusky *et al.* 2000, 2003) of right lateral motion between the two plates. In its eastern part, the surface expression of the NAF is relatively narrow and simple. At the neighbourhood of the Marmara Sea it splays into several branches. The northern branch of the NAF within the Sea of Marmara accommodates about 80 per cent of the displacement forming a complex fault system.
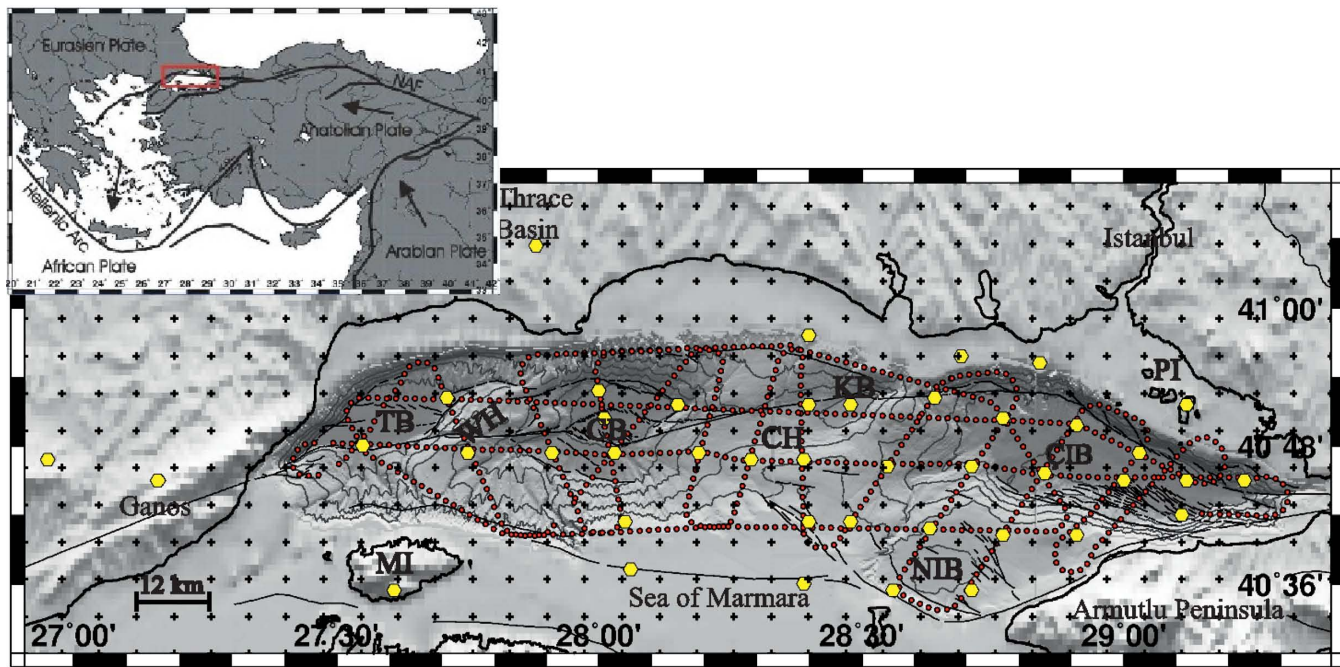
Figure 1. Location map of the SEISMARMARA-Leg1 survey at the North Marmara Trough within the Sea of Marmara. Yellow hexagons are the receivers (OBSs and land stations) of the survey network. Only the land stations used for this tomographic study are shown. Red points are picked shots. Every 1/10 shots have been picked and there is 1500 m distance between two picked shots. Grey contours are the isobaths of 200 m interval of the multi-beam bathymetry acquired by *R/V Le Suroit* (Le Pichon *et al.* 2001; Armijo *et al.* 2002) within the North Marmara Trough. The submarine faults scarps after Armijo *et al.* 2002 are represented in black. The black crosses are the nodes of the inversion grid. In the horizontal directions (in x and y), there is 6 km distance between grid nodes. TB, Tekirdag Basin; MI, Marmara Island; WH, Western High; CB, Central Basin; CH, Central High; KB, Kumburgaz Basin; NIB, North Imrali Basin; CIB, Çınarcık Basin. The inset shows the tectonic settings of the region after Hergert & Heidbach (2010).

The Marmara Sea is a marine basin located south of Istanbul (Fig. 1). It comprises a shallow shelf to the south and a deeper northern part called the North Marmara Trough (NMT). The NMT is affected by three pronounced bathymetric depressions with depths (bsl) over 1200 m, called from west to east, the Tekirdağ, the Central and the Çınarcık basins. Three basins are separated from each other by two NE-oriented bathymetric highs called the Western and the Central highs.

The NAF has ruptured during a well-known westward-propagating earthquake sequence between 1939 and 1999 (Toksoz *et al.* 1979; Barka 1996; Stein *et al.* 1997; Nalbant *et al.* 1998; Pondard *et al.* 2007). Currently the western tip of this sequence is located in the Marmara Sea region. The Marmara Sea forms a seismic gap between the Izmit strike-slip segment to the east, which ruptured in 1999 by two destructive earthquakes: Izmit (M_w 7.4) and Düzce (M_w 7.2) and the Ganos strike-slip segment to the west which ruptured in 1912 Mürefte (*M* 7.4) earthquake.

Numerous onshore and offshore scientific investigations including geological (Yaltirak 2002; Okay *et al.* 2004; Sengor *et al.* 2005; Yilmaz *et al.* 2010), seismological (Taymaz 2000; Karabulut *et al.* 2003; Sato *et al.* 2004; Taymaz *et al.* 2004; Vanacore *et al.* 2013), GPS (Reilinger *et al.* 1997; Straub *et al.* 1997; McClusky *et al.* 2000; Flerit *et al.* 2003), multibeam bathymetry (Le Pichon *et al.* 2001; Armijo *et al.* 2002, Armijo & the Marmarascarps Cruise Party 2003), coring and MCS profiles (Ergun & Ozel 1995; Smith *et al.* 1995; Wong *et al.* 1995; Aksu *et al.* 1999; Okay *et al.* 1999, 2000; Imren *et al.* 2001; Le Pichon *et al.* 2001; Parke *et al.* 2002; Demirbag *et al.* 2003; Laigle *et al.* 2008; Bécel *et al.* 2009, 2010; Grall *et al.* 2012) have been carried out in the past in the Marmara Sea region. The studies before the 1999 earthquakes were mainly focused on the Marmara Sea basin development. The 1999

earthquakes motivated the scientific community to investigate the northern fault system within the Marmara Sea in order to evaluate its nature and activity. These studies have captured essential elements of the general picture but due to the penetration limitation, they could not provide a detailed image of basement topography in this region. Therefore, until now thickness variations of the brittle part of the crust could not be taken into account in the estimation of the seismic potential of the region. Due to the complexity of the fault system and to the absence of *a priori* information on the 3-D heterogeneity of the upper-crustal structure, several rupture scenarios with magnitudes varying between $M = 7.2$ and 7.6 have been proposed for this region (Hergert & Heidbach 2010, 2011).

1.2 Seismic experiment

The SEISMARMARA-Leg1 seismic survey was a French-Turkish project carried out with the R/V le Nadir, in 2001, after the 1999 Izmit and Düzce earthquakes. Its aim was to investigate the seismic structure and activity of the NMT at the crustal scale. During the survey a total of 2000 km MCS profiles have been acquired. They have an unprecedented penetration due to the 4.5 km length 360 channel digital streamer and to the strength of 8100 or 2900 cu.in. airgun array tuned in single-bubble mode (Avedik *et al.* 1995, 1996). Laigle *et al.* (2008) have identified the boundary between syn-kinematic sediments deposited after the propagation of the NAF into the Marmara Sea region and the older pre-kinematic strata, called pre-kinematic basement, as a highly reflective interface on the MCS profiles. The study of MCS profiles revealed the general architecture and the upper-crustal structures of the Çınarcık and the Central basins and the deep structure of the southern shelf of the NMT. It has

shed light on variations of the basement above a gently shallowing Moho mirrored by the top of the lower crust beneath the NMT.

During the survey additional wide-angle data has been recorded by 37 three-component ocean-bottom seismometers (OBS) from ISV Hokkaïdo (Japan) and a same amount of temporary short band land stations with three components. These instruments recorded continuously over 1.5 month (in average) the natural seismicity and shots. OBSs have been deployed and collected by the Turkish MTA's ship Sismik-1. The WARR modelling along 2-D profiles on both, OBS and land stations revealed the deep structure under the NMT itself. It allowed extending the discussion on crustal thinning under the central NMT and quantifying the crustal deformation (Bécel *et al.* 2009). By combining the high resolution pre-stack depth migration of seismic lines for the shallow part with the forward modelling of OBS arrival times of refracted waves within the basement, Bécel *et al.* (2010) identified the non-reflective crystalline basement which forms the boundary between the pre-kinematic strata and the crust along a set of selected lines.

In this paper, we examine the 3-D *P*-wave velocity structure of the Marmara Sea through the sedimentary cover down to the crystalline basement by using active source first arrival time data. Due to the spacing between shot profiles, the final 3-D view of the basement obtained by the 3-D first arrival time tomography will be smoother than along 2-D profiles when the basement is seen. However, in the well-cross sampled parts of the NMT, the upper-crustal information provided by the *P*-wave data reveals the variations of the basement depth in three-dimensions and thus helps to characterize the basement depth which is generally considered as a proxy for the top of the seismogenic zone.

Similar controlled source 3-D first arrival time tomography studies have been carried out in the past with various inversion codes dedicated to this purpose (e.g. Zelt & Barton 1998; Hobro 1999; Hobro & Sing 1999; Hobro *et al.* 1999; Koulakov *et al.* 2007). One of the specific aims of this study is to obtain a 3-D initial model for the future local earthquake tomography (LET). Hence, for the 3-D controlled source tomography we use the code Simulps dedicated to LET (Thurber 1983, 1993; Eberhart-Phillips 1990, 1993; Evans *et al.* 1994) and which can invert additional shots and blasts that would have been recorded during the survey (e.g. Dinc *et al.* 2010; Eberhart-Phillips & Bannister 2010; Yolsal-Çevikbilen *et al.* 2012). We present the results obtained with the controlled source data set to infer the supracrustal heterogeneity. In a future stage, the final model obtained by this study will be integrated into the joint inversion of local earthquakes and controlled source data by using the same parametrization and the same code.

1.3 Data set

We used the *P* wave first arrival time data from the shot profiles acquired with the large 8100 cu.in source which has a time window 60 s that allows to pick the first arrival times without being disturbed by the signal of the next shot. The data involves four E–W lines and 13 cross-lines with various azimuths, covering the whole NMT (Fig. 1). In order to sense the dips of the reflectors, the survey has been designed to have OBSs at crossing points of profiles and land stations placed at the end of the profiles. This geometry is also very suitable for the 3-D artificial shot tomography since all these shots have been recorded by the OBSs, which remained at the sea bottom for 1.5 month. The *P*-wave data from in-line and off-line profiles cross-sample abundantly the top of the crust and the sedimentary cover of the Marmara Sea.

Shot recordings have been gathered into profiles and analysed on receiver gathers. First arrival times have been picked by analysing them visually. No frequency filtering has been applied for pickings. Each shot profile has been picked on each 35 OBS of the network and on five land stations chosen regarding their positions. Along shot profiles every 1/10 shots have been picked with a spacing of 1500 m between two picked shots. This interval between picked shots is still much smaller with respect to the distance between receivers and between profiles (approximately 10 km), which is one of the parameters to be considered for the medium parametrization by the inversion grid. We considered the first arrival times which correspond to either direct waves for near offset traces or refracted waves within sedimentary layers and the basement depending on the offset. Secondary arrivals such as reflected waves on the basement have not been considered.

First arrival times could be picked until 100 km offsets (Fig. 2). On the record sections, reflected waves off the Moho (PmP) were visible but not considered since they are not first arrivals. Refracted waves from Moho (Pn) were only observed on the few OBSs located on the southern shelf. The final data set contains more than 16 000 first arrival times, which are mostly refracted waves at the top of the basement within the crystalline part of the crust (Pg). Weights from 0 to 3 have been attributed to first arrival readings according to the signal to noise ratio (Fig. 2), which vary with distance due to the attenuation or due to the undesirable noise such as ships, blasts or signals from earthquakes. The standard error of the measurements are assumed to be ±25, 50 and 100 ms corresponding to the quarter of a period, the half of a period and one period for the 1, 2 and 3 weighted shots, respectively. Accordingly, the estimated variance due to the reading uncertainty of the present data set is 0.002 s^2. The representation of the seismograms in receiver gathers which provide a visual coherence allows the minimization of the picking errors. We also checked the accuracy of the pickings with the principle of inverse return of light on a homogeneously distributed small subset of data (shots located over OBSs).

2 3-D INVERSION OF THE CONTROLLED SOURCE DATA SET

The Simulps algorithm developed by Thurber (1983, 1993) and Eberhart-Phillips (1990, 1993) has been used for the present controlled source first arrival time inversion for 3-D *P*-velocity structure. The Simulps code is more commonly used for LET studies with the possibility to jointly invert additional controlled source first arrivals. It computes the inverse solution for *Vp* and *Vp/Vs* and relocates hypocenters in the updated velocity model using the iterative damped least squares technique. In this study, we chose to start with the shot inversion, since we had recorded too few earthquakes for deriving the tremendous heterogeneity of the upper crustal structure. In this original case, the data set contains only first arrival times of shots with known origin times and locations and thus the only unknown parameters are medium velocities. This configuration offers a more homogeneously distributed data set and there are less unknown parameters than in LET. However, in order to represent accurately the most heterogeneous part of the crust that is the supracrustal structure, consideration has to be given to the medium parametrization during the inversion procedure.

2.1 Parametrization of the medium

In the code Simulps medium velocities are defined at the nodes of a 3-D grid, which are located at intersections of three orthogonal
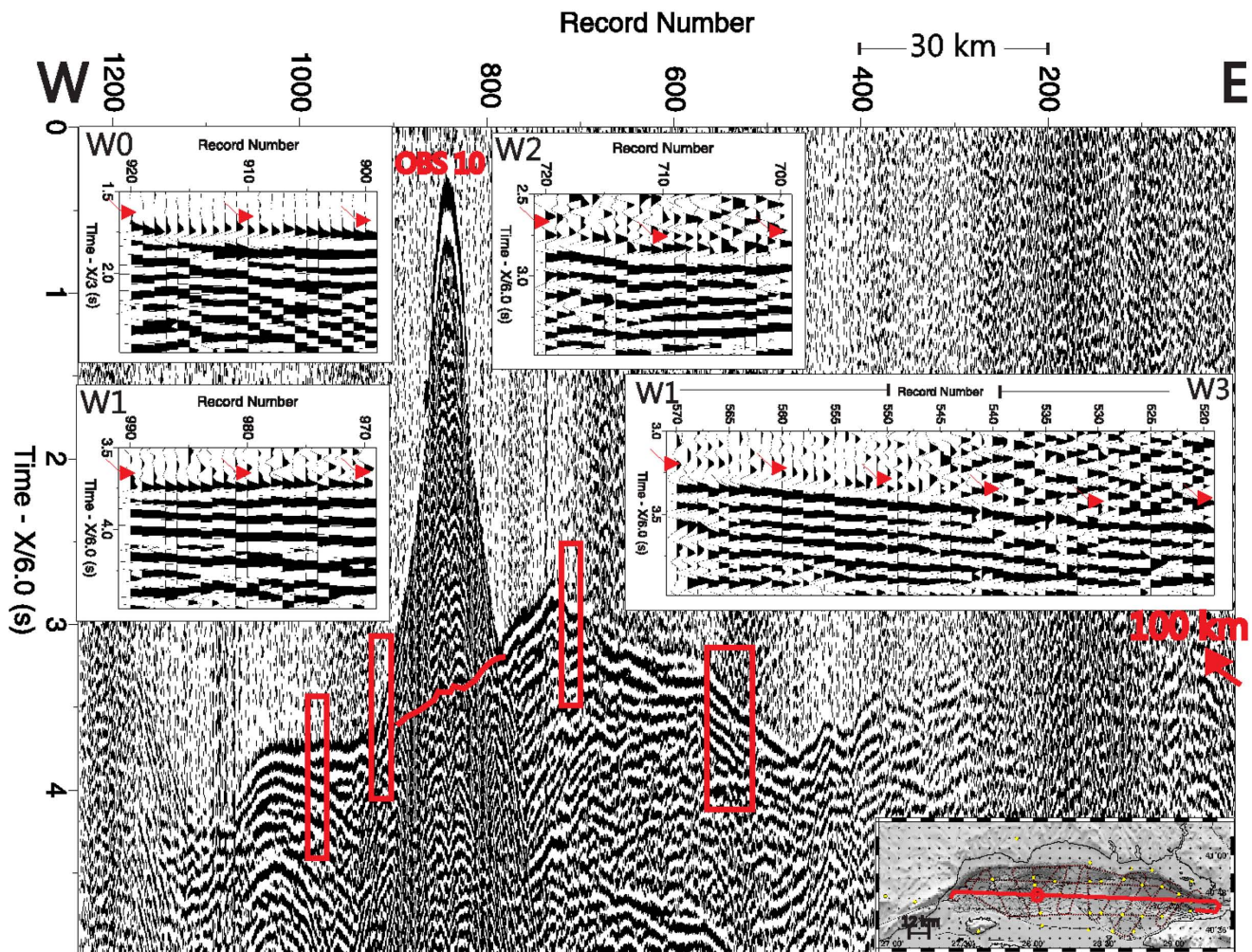
Figure 2. Seismograms of shots along the E–W shot profile (profile 1) which cuts across the middle part of the NMT recorded by the in-line OBS 10 located within the Central Basin. The position map shows the location of the OBS10 (red circle) and the profile 1 (red line). Inset seismograms show signals with different weights varying from 0 to 3. Red arrows on inset seismograms show the first arrival pickings. A velocity reduction of $3\,km\,s^{-1}$ is applied for the seismograms of zero weighted shots corresponding here to diving waves in sediments. A velocity reduction of $6\,km\,s^{-1}$ is applied for other seismograms. Red rectangles show the location of zooms. A bandpass filter of 3–15 Hz and a constant gain over the whole data set are applied to seismograms. Reflections from the acoustic basement are shown in red line.

planes. Velocities vary continuously in all directions with linear B-spline interpolation. Ray paths are either computed using an approximate 3-D ray tracer with pseudo bending (ART-PB, Um & Thurber 1987) or with shooting method (RKP, Haslinger 1998; Haslinger & Kissling 2001). For this study both ray tracing methods have been tested and resulting ray paths were nearly identical. Haslinger & Kissling (2001) have shown that indeed the two ray tracing methods yield different ray paths especially for events with larger offsets than 80 km. In this study, to avoid the introduction of artefacts, which may occur due to the mainly horizontal ray sampling in deeper layers, shots with offsets larger than 80 km have not been inverted. Therefore, the ART-PB algorithm, which requires less computational time has been preferred for presented inversions. The choice of other control parameters like the damping, maximum velocity adjustment allowed per iteration and the number of iteration are explained in the Appendix.

The grid node spacing has been chosen to allow uniform distribution of the resolution trough the medium. The interval between grid nodes depends on the survey geometry. The 10 km distance between shot profiles and receivers of the SEISMARMARA survey allows us to have at minimum $6 \times 6\,km$ parametrization in horizontal directions (in x and y-axes). Due to the mainly vertical ray propagation at the shallower layers, a denser horizontal parametrization would yield inhomogeneous resolution distribution with under-sampled nodes at the shallower layers. The E–W oriented x-axis of the inversion grid was chosen to be parallel to the NMT borders and to the E–W shot profiles (Fig. 1). The inversion grid has 40 and 17 nodes in x and y directions, respectively. In depth (along the z-axis), 16 nodes with 2 km spacing between -2 and 26 km depth, and one last node at 100 km depths, with zero value corresponding to the sea level and the values being positive downwards. Accordingly, the depth refers to below the sea level (bsl) here after The present data set of 16 000 first arrival times would allow a denser parametrization in depth. However, with such parametrization, due to the horizontal node interval getting too large with respect to the vertical one the ray distribution would be mainly in one direction.

Grid node velocities at depths greater than 12 km have only been used for the computation of the forward solution. Their velocities have been interpreted from the 2-D refraction profiles and these nodes within the lower-crustal part have been kept fixed during the inversions. Additionally, nodes with a derivative weighted sum (the number of rays normalized by their length and distance to the node),

(DWS) <50 at depths <12 km have been kept fixed in order to avoid artefacts due to the low cross-sampling.

2.2 The choice of initial velocity model

Previous MCS (Laigle *et al.* 2008) and WARR 2-D (Bécel *et al.* 2009, 2010) profiles have revealed depth variations of the basement of up to 7 km between the NMT and its surroundings. They also revealed variations of 2 km occurring in distances smaller than 4 km within the trough itself, in a non-cylindrical way along the NMT axes. A tomographic inversion with a 3-D initial model is more appropriate than a 1-D or even 2-D models to represent such variations. However, the accurate representation of such a medium onto a 3-D initial model requires a good *a priori* knowledge of the topography of the main interfaces, which is not the case everywhere in the NMT since we have only constraints on the basement depth along localized profiles. An unrealistic 3-D initial model may lead to a worse solution than a 1-D model since it may bias the solution in a specific way (Kissling *et al.* 1994). Therefore, despite the expected large amplitude of the velocity perturbations, we have first tested several 1-D initial models in order to have a feeling of the physically possible solutions.

Two of the tested 1-D initial models representing different parts of the Marmara Sea are shown in Fig. 3. One of them represents the velocities within the NMT itself (called the 'NMT model' hereafter), whereas the other one represents the velocities of its margins. In the NMT model the acoustic (corresponding to the P-wave velocity of 4.5 km s^{-1}) basement is nearly at 4 km depth. This could be seen as an average basement depth between the deep basins and the basement highs. In the margin model, it is at 1 km depth representing the basin borders where the pre-kinematic basement outcrops.

Inversion tests with 1-D initial models have been run with a subset of data containing the first arrivals with smaller offsets than 50 km. Larger offset arrivals have not been inverted to avoid artefacts due to the mainly horizontal ray propagation (without ray crossing) at deeper layers. Given that 50 km is much larger than two times the interval between OBSs and between shot profiles ($\sim$10 km), rays within this offset limit have been judged large enough for having abundant ray crossing at the supracrustal part. This subset of data contains more than 11 000 *P*-wave first arrival times.

After having analysed the damping *value* and the required number of iterations (see the Appendix for the choice of control parameters), a six-iteration inversion with a damping of 70 has been run with the NMT model whereas the 'margin model' needed 17 iterations with a damping value of 500. Inversions with both models lead to very high reduction in data variance (the NMT model: 96.5 per cent and the margin model 99.2 per cent) and the final data variances are 0.02 and 0.03 s^2 for trough and margin models, respectively. Surprisingly, regardless the fact that the two chosen initial model are very different, in the centre of the study volume the retrieved solutions are very similar (Figs 3c and d). Both inversions have constrained the main structural elements of the Marmara Sea. However, none of the two inversions led to a realistic solution at the NMT borders located outside of the network. On the results with the trough model, the offshore nodes at NMT borders and the onshore ones appear with too low and unrealistic velocities. On the contrary, due to the sparse ray sampling, the margin model yields artefacts with very high velocities (<8 km s^{-1} at 2 km depth) at the northern border of the Çınarcık Basin. Both inversions ended up with very large perturbations with respect to the initial model reaching up to 50 per cent at shallower layers (Figs 3e and f). In some other geodynamical contexts such large perturbations could be considered

as artefacts but in the Marmara Sea they were expected, because a unique 1-D initial model cannot represent the velocities of the NMT borders with an outcropping basement as well as the velocities of the NMT itself. Such large perturbations may produce some leakage at the under resolved part of the medium and consequently they may perturb the retrieved basement topography. Therefore, before any interpretation, the assessment of the reliability of the retrieved structure is considered and established hereafter.

3 QUALITY ASSESSMENT

An inversion with synthetic first arrival times computed through a characteristic model is run in order identify the well-resolved nodes on the results and to quantify the amount of leakage. The characteristic model, as described by Haslinger *et al.* (1999); Husen *et al.* (2000) contains anomalies of a similar size and amplitude as the real ones but with different strikes, shapes. Inverse signs have been considered in the specific case of earthquakes where the ray paths are less certain due to the unknown source locations. For the present synthetic test, a characteristic model is prepared by perturbing the 1-D trough model at 4 and 6 km depths with anomalies which amplitudes and shapes are similar to the real structure (Fig. 4). In order to identify the amount of leakage, the other layers have not been perturbed and the anomalies injected at 4 and 6 km depths are not continuous in depth, they have different shapes. The injected anomaly amplitudes decrease with depth as observed for the real anomalies. At 4 and 6 km depth they are up to 30 and 20 per cent, respectively.

The synthetic first arrival times computed through this model are inverted with the NMT model by using the same control parameters as the real inversion. The synthetic inversion results are compared with the injected pattern (Fig. 4). At 4 and 6 km depths, besides the westernmost part of the study area, the injected pattern is totally retrieved beneath the shot and receiver network. The lack of the resolution at the westernmost part of the study area is due to the failure of OBS 13. We analysed the resolution matrix of the synthetic inversion. The thresholds values of the diagonal element of the resolution matrix (RDE) and the spread function (SF; Michelini 1991; Michelini & McEvilly 1991) have been chosen by identifying the nodes where the injected pattern is accurately retrieved and by discarding the ones where the leakage is up to 10 per cent. The shapes of the contours of RDE and SF threshold values of the synthetic inversion are exported on the real inversion. RDE and SF values of the nodes remaining within the exported contours are analysed and the threshold values of the real inversion are estimated by this analysis.

The synthetic inversion showed that, some leakage reaching up to 10 per cent can be observed by starting the inversion with a 1-D model. Moreover, due to the lack of cross-sampling, none of the 1-D models yield a realistic solution beneath the NMT margins. These inversion tests with 1-D initial models pointed out the need to use a 3-D initial model since we aim at using the resulting model for other applications (e.g. as initial model for the earthquake relocation and for the geomechanical modelling studies), which need reasonable velocities even in areas of low seismic resolution.

4 ELABORATION OF THE 3-D *a priori* VELOCITY MODEL

We developed an approach to build a realistic 3-D initial model by introducing the available *a priori* structural information that is
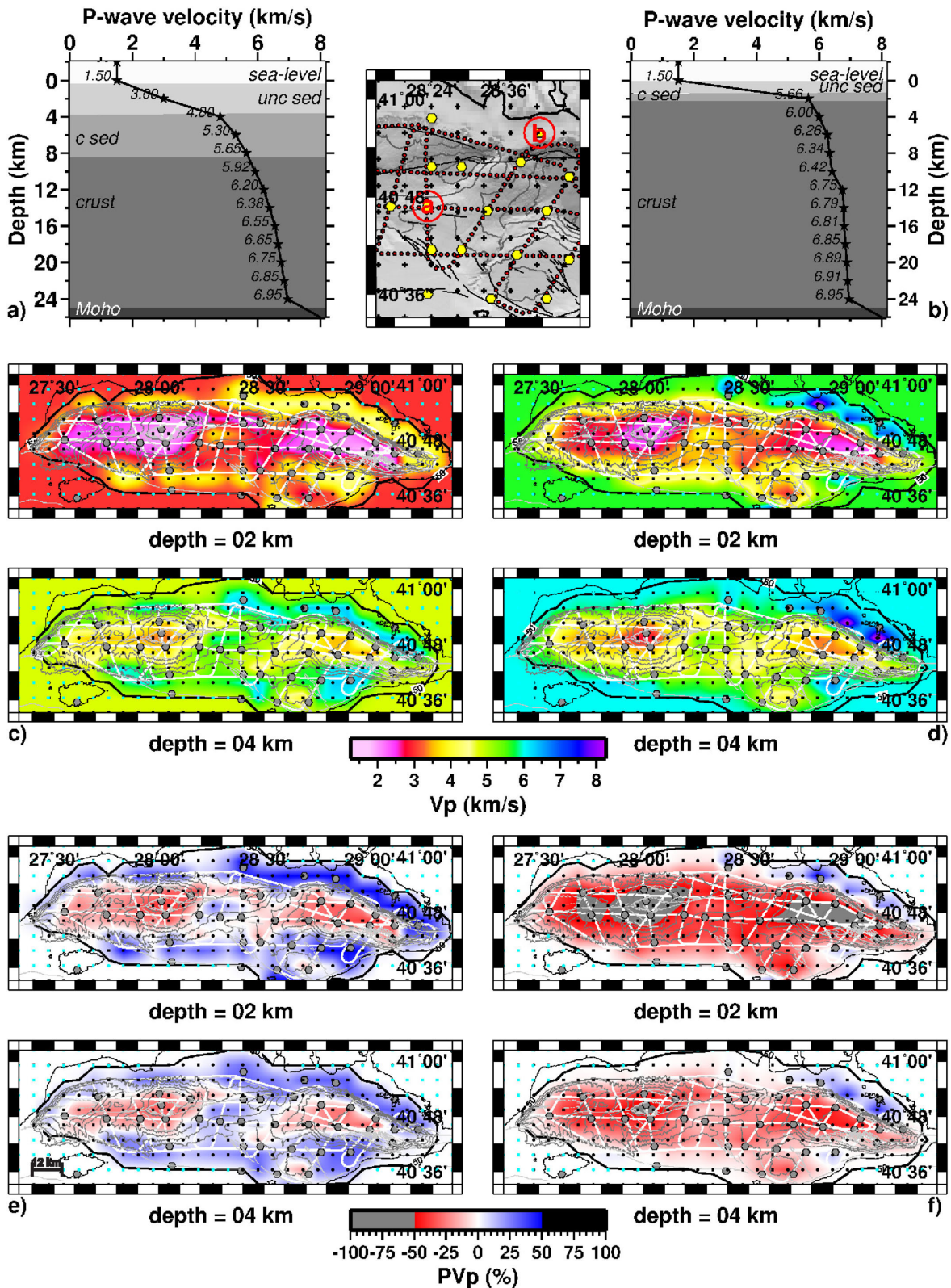
Figure 3. (a) Trough model: 1-D initial model representing the velocities beneath the Central High. unc sed, unconsolidated sediments; c sed, consolidated sediments. (b) Margin model: 1-D initial model representing the velocities beneath the northern border of the Çınarcık Basin. (c) The six iterations inversion (damping = 70) results with the 1-D initial model representing the velocities of the trough. (d) The 17 iterations inversion (damping = 500) results with the 1-D initial model representing the velocities of the margins. (e) *A posteriori* percentage velocity perturbations with respect to the trough model. (f) *A posteriori* percentage velocity perturbations with respect to the margin model. Black contours surround the nodes with higher dws values than 50, which are inverted nodes.
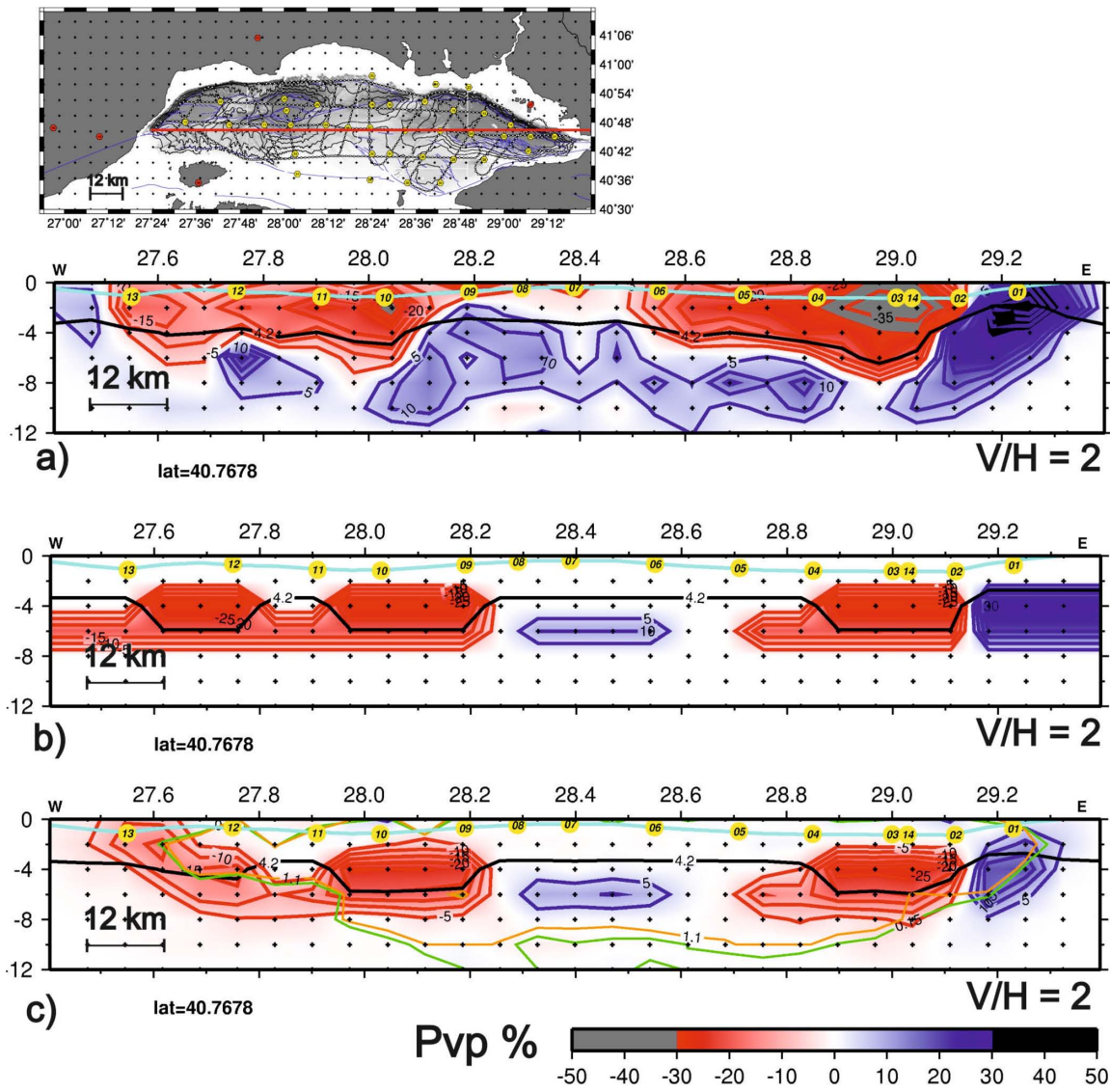
Figure 4. (a) *A posteriori* percentage velocity perturbation with respect to the trough model (Fig. 3a) along the E–W cross-section which cuts across the middle part of the study volume. Yellow circles indicate OBS locations along the cross-section. The seafloor bathymetry is shown in blue line. The black contour is the iso-velocity contour of $4.5 \, \text{km s}^{-1}$, which is used as a proxy to the pre-kinematic basement. Vertical exaggeration is 2. (b) Characteristic model containing anomalies of similar size and amplitude as the ones obtained by the real inversion. Amplitudes of injected anomalies are up to 30 per cent at 4 km depth and decrease with depth. 0, 2, 8 10 and 12 km depths have not been perturbed for the identification of the possible leakage. (c) The synthetic inversion result. Contours of RDE and SF threshold values surrounding well resolved areas are represented in green and in orange, respectively. The position map shows the location of the cross-section.

the topography of the main interfaces: the seafloor bathymetry, the pre-kinematic and the crystalline basements and the Moho.

The detailed map of seafloor bathymetry covering the whole NMT was available from a previous multibeam survey (Le Pichon *et al.* 2001; Armijo *et al.* 2002). For the northern and southern shelves of the NMT at depth between 0 and 100 m, a seafloor depth of 100 m has been considered. Velocities of the sedimentary infill, from the sea-bottom deposits ($1.6 \, \text{km s}^{-1}$) down to the base of the Pliocene–Quaternary syn-kinematic sediments ($3.9 \, \text{km s}^{-1}$), have been provided by the velocity analysis along the MCS profiles (Laigle *et al.* 2008; Bécel *et al.* 2010).

Topographies of the pre-kinematic and crystalline basements have been provided from the MSC and WARR profiles (Bécel 2006; Laigle *et al.* 2008; Bécel *et al.* 2009, 2010). This *a priori* information was only available along a set of 2-D profiles with different azimuths. Additional information on the depth of basement

below the OBSs have been obtained by analysing two-way travel-times (twt) of the reflected waves at zero offset (Fig. 2) and the basement depth have been approached by transforming the twt, in depth with an average velocity of $3 \, \text{km s}^{-1}$ for the whole sedimentary thickness. When the pre-kinematic basement topography was not available either by the previously studied 2-D profiles or by the zero offset reflections, the results of the previous inversion with the 1-D margin initial model have been used to fill the gaps. Obviously, tomographic results have only been considered at the well-resolved areas confirmed by the synthetic tests. Once the *a priori* topography has been established, the pre-kinematic and the crystalline basement interfaces have been represented in the 3-D initial model by velocity steps from 3.9 to $4.5 \, \text{km s}^{-1}$ and from 4.9 to $5.7 \, \text{km s}^{-1}$, respectively.

For the nodes located onshore we have considered the structural information provided by the geological map of the Marmara Sea region (Yaltirak 2002; Yilmaz *et al.* 2010).

Accordingly, besides its northwestern part which corresponds to the Thrace Basin, the surroundings of the Marmara Sea with an outcropping Pre-neogene basement are represented in the 3-D model with crustal velocities (5.7 km s^{-1}) at 0 km depth. The Thrace Basin, which is located at the north-western part of the region, is considered as being the fore-arc basin of the Intra-Pontide collision (Sengor *et al.* 2005) and it is covered by thick Early Miocene–Early Pliocene detritic sediments. In the 3-D initial model, the sedimentary cover of the Trace Basin has been locally represented with lower velocities (∼4 km s^{-1} at 0 km depth) injected beneath land stations located into the basin. Since land stations are far from the shot network of the survey (at offsets larger than 40 km), the rays corresponding to the shots recorded by these stations propagate mainly into the deeper layers where the velocity variations are smaller. It is only immediately below stations that the corresponding rays propagate vertically within the sediments of the Thrace Basin. The injected velocities have been decided by analysing the *a priori* residuals of these stations.

The Moho depth beneath the NMT (at 26 km depth) has been provided by WARR modelling study along two regional E–W profiles and a N–S profile (Profile 5) from the far offset recordings on land stations (Bécel *et al.* 2009). The Moho interface has been represented by a velocity step from 7 to 8 km s^{-1} into the 3-D initial model.

Along every constant *x*-axis of the 3-D inversion grid, 2-D cross-sections have been compiled by the combination of the above-mentioned information. At each node position along the 2-D constant *x*-axis cross-sections, velocities have been resampled in the depth with 2 km intervals corresponding to depths of nodes along the *z*-axis of the 3-D grid (Fig. 5).

In order to check the representation of the topography of interfaces into the 3-D inversion grid, the iso-velocity contours corresponding to velocities at both sides of the injected interfaces have been plotted and compared to the 2-D refraction profiles of Bécel *et al.* (2010) (Fig. 5). For each injected interface an iso-velocity contour that can be used as visual guide for the interpretation of the results has been identified. This analysis has shown that the 4.2 and 5.2 km s^{-1} iso-velocity contours represent accurately the topography of the pre-kinematic and crystalline basements, respectively. This verification has also shown that due to the interpolation between nodes, the zones where the pre-kinematic basement outcrops beneath a thin water layer cannot fully be represented by the actual inversion grid with 2 km node interval along the *z*-axis (Fig. 5). During the interpretation of the results we will be careful to such systematic errors and we will refer to this specific case with the appellation 'the shallow sea-bottom and the outcropping basement case'.

Thanks to the accurate representation of on-shore velocities with this 3-D initial model, first arrival time picking from five land-stations has been added into the inverted data set to improve the resolution at the borders of the NMT, especially at the westernmost part of the study volume. The inversion has been run by considering first arrival times of shots of up to 80 km offsets. The *a priori* residuals with the 3-D model are on the order of one second, significantly smaller than with 1-D models (trough model: ±2 s and margin model: −0.5 to 3.5 s). Before the inversion with the 3-D initial model the analysis for the damping and the required number of iteration has been repeated with the larger data set (see the Appendix). Accordingly, an inversion of 4 iterations with a damping value of 150 has been run. During this inversion, the nodes with low cross-sampling and consequently with low resolution which have been identified by the previous synthetic test have been kept fixed.

They have only been used for the computation of the ray paths and the travel times along the paths.

At 2 km depth, final perturbations with respect to the 3-D initial model are only locally up to 15 per cent. The average perturbations with respect to the 3-D initial mode are −6.7/8, −3.66/7.87 and −3.26/5.53 per cent at 2, 4 and 6 km depths, respectively (S2). The inversion produces 74 per cent of reduction in the data variance and the final data variance is 0.02 s^2, which is still larger than the expected variance due to the reading error (0.002 s^2).

5 RESOLUTION TEST AND COMPARISON WITH 2-D METHODS

5.1 Checkerboard test

In order to check the spatial resolution of the actual data set we performed a checkerboard test as defined by, Zhao *et al.* (1992), Lévèque *et al.* (1993), Spakman (1993), Benz *et al.* (1996), Zelt & Barton (1998), Zelt *et al.* (2001) and Tong *et al.* (2003). We chose the amplitude and the size of the anomalies in the checkerboard pattern by analysing the *a posteriori* percentage perturbations with respect to the 3-D initial model of the real data inversion (Fig. 6a). Accordingly we run the synthetic test with a checkerboard pattern containing blocks of 12 km × 12 km × 6 km dimensions alternating high and low velocity anomalies of ±5 per cent amplitude (Fig. 6b, see also Figs S3 and S4). The checkerboard pattern has been injected at 2, 4 and 6 km depths. The nodes at 0, 8 and 12 km depths are not perturbed for the identification of the possible leakage which may occur due to the ray sampling that could be mainly in one direction (without cross sampling) at these depths. To simulate the real conditions, a random noise in the same order as the real travel time residuals has been added to the synthetic first arrival times.

Beneath the area covered by the shot and receiver network, the injected checkerboard pattern is accurately retrieved with amplitudes similar to injected ones. The slight decrease at the amplitudes of the retrieved anomalies with respect to injected ones is due to the conservative (high) value of the applied damping factor. Although additional data from the land stations increase the ray sampling, this part of the study volume remains less well resolved compared to the rest of the 3-D volume. As done for the previous inversions with 1-D initial models, accurately resolved nodes are identified by comparing synthetic inversion results with the injected checkerboard pattern. On the following inversion results, the contour of 0.2 and 0.05 of the RDE will be plotted on the results in order to represent the zones where the resolution is good and acceptable, respectively. The area with lower RDE values than 0.05 will not be interpreted.

5.2 3-D *P*-wave velocity heterogeneity

The map view of 2, 4, 6 and 8 km depths of the 3-D *Vp* heterogeneity model obtained by the controlled source inversion is shown on the Fig. 7. The NMT and its borders appear with contrasted velocities. Within the three deep basins of the Marmara Sea (seafloor depth >1200 m) low *P*-wave velocities corresponding to the sediments (1.8–4.2 km s^{-1}) are observed down to 6 km depth. The North Imralı Basin located on the southern platform, southwest of the Çınarcık Basin, appears also with sedimentary velocities down to at least 4 km depth. The seafloor depth is only 400–500 m in this basin. Thus, the sedimentary thickness within this basin appears to be nearly as thick as its northern neighbour. The North Imralı and the Çınarcık basins are separated from each other by an E–W basement
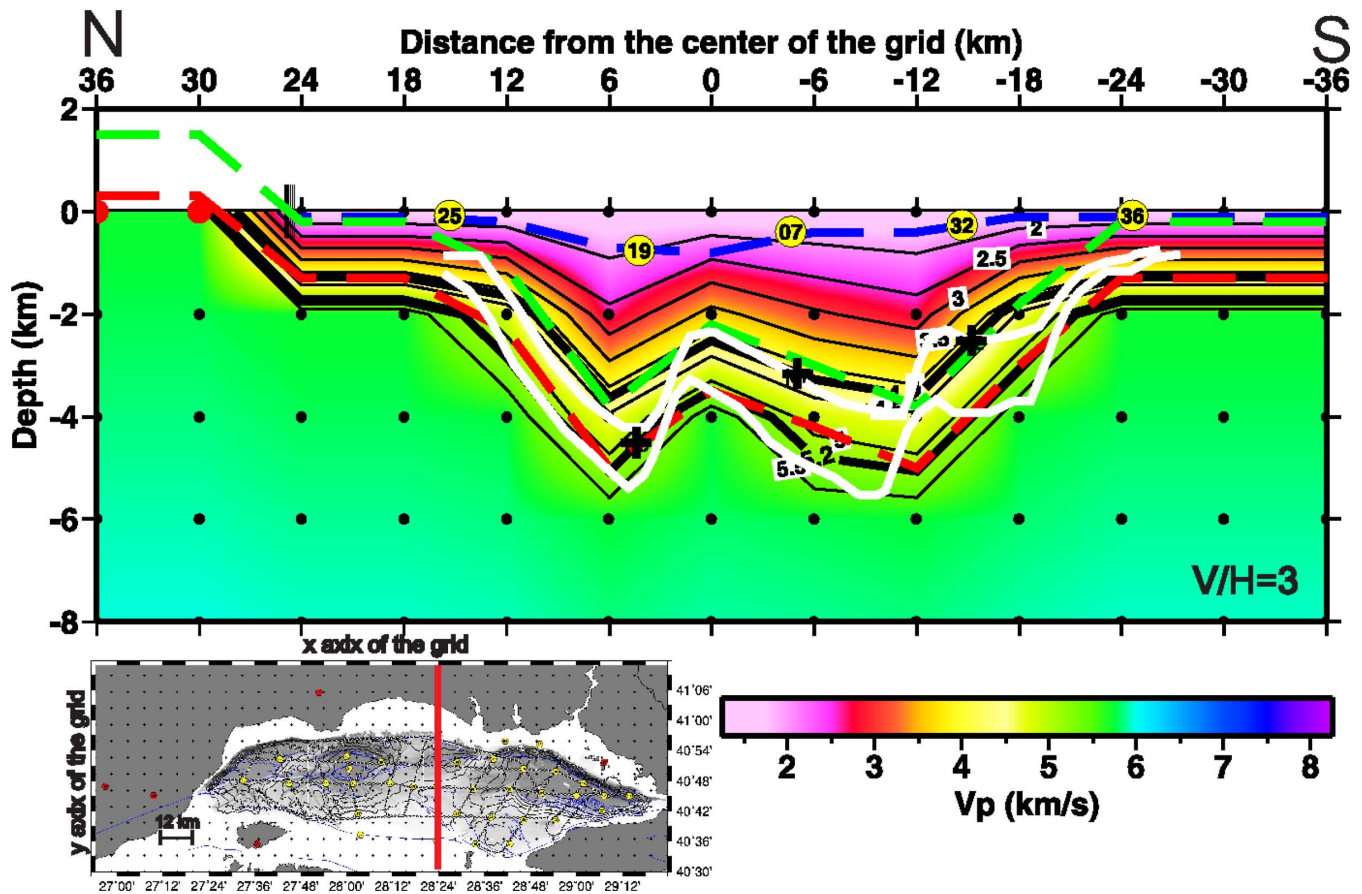
Figure 5. The cross-section trough the 3-D initial model, along the longitude 28.3281° corresponding to the $x = 15$ axis of the inversion grid. It illustrates the considered *a priori* information for building the 3-D initial velocity model. The position map shows the location of the cross-section. Along the cross-section, yellow circles are the in-line OBSs. White contours are pre-kinematic (top) and crystalline basements (bottom) retrieved by wide-angle reflection, refraction modelling (Bécel *et al.* 2010) along the same profile. Black crosses illustrate the basement depth approached with reflected waves at zero offset beneath OBSs. Dashed blue, green and red lines are the considered topography of the seafloor bathymetry, the pre-kinematic basement and the crystalline basement, respectively. Thick black contours are iso-velocity contours of 4.2 km s^{-1} (top) and 5.2 km s^{-1} (bottom) which mimic considered pre-kinematic and crystalline basement topographies. Black points are nodes of the inversion grid. Vertical exaggeration: 3

high which is identified by its high velocities which contrast with the basins velocities. Between the Central and the Çınarcık basins, the Central High is characterized by high velocities, close to 5.5 km s^{-1} at 4 km depth. To the north, the high velocities of the Central High are bounded by a narrow zone of low velocity, which is approximately located beneath the seafloor trace of the NAF. This negative anomaly is best observed on the slice map at 4 km depth with a velocity of 4 km s^{-1} contrasting with the 5.5 km s^{-1} of velocity of the Central High. A similar narrow zone of low velocity is observed south of the Central High, also with a velocity of 4 km s^{-1} at 4 km depth. Contrarily to the Central High, the Western High does not appear as a velocity contrast between the Central and the Tekirdağ basins. It can only be identified on the high-resolution bathymetric map (Fig. 1). Beneath the bathymetric expression of the Western High low velocities have been observed down to 6 km depth. This suggests that the Western High is not a basement high but it is a relief formed by the sediments. The Central and the Tekirdağ basins appear thus linked, forming a 60-km-long zone of low velocities.

In the following, the above mentioned findings will be discussed along vertical cross-sections where the tomographic results are compared with the 2-D WARR and MCS profiles. Some of MCS profiles acquired during the SEISMARMARA survey leg-1 have been depth migrated (Laigle *et al.* 2008; Bécel *et al.* 2009, 2010). The vertical velocity filed used for the depth migration of MCS profiles consists

in the velocities of successive layers in depth. Such velocity field may contain velocity inversions due to the low velocity layers. But in the refraction studies velocities increase smoothly in depth and the low velocity layers are not considered. In order to avoid a biased comparison, we do not directly compare the depth migrated MCS profiles with the tomographic results but we will transform the tomographic results in twt in order to compare them with the MCS profiles (e.g. White *et al.* 2008).

5.3 Eastern third of the study volume: Çınarcık and North Imralı Basins:

The N60°E oriented high resolution seismic profile SM36 is orthogonal to the NE border of the Çınarcık Basin to the north and it cuts across eastern part of the North Imralı Basin to the south (Figs 8a and b). On the tomographic results (Fig. 8a) the 4.2 km s^{-1} iso-velocity contour reflects the basement expressions of the Çınarcık and the North Imralı basins as well as the basement high, which forms the southern border of the Çınarcık Basin and separates the two basins. The NE border of the Çınarcık Basin is marked by a lateral velocity contrast, which happens within 6 km distance and it can be observed down to 6 km depth. On the time section superimposed on the MCS profile (Fig. 8b), the location of this velocity contrast
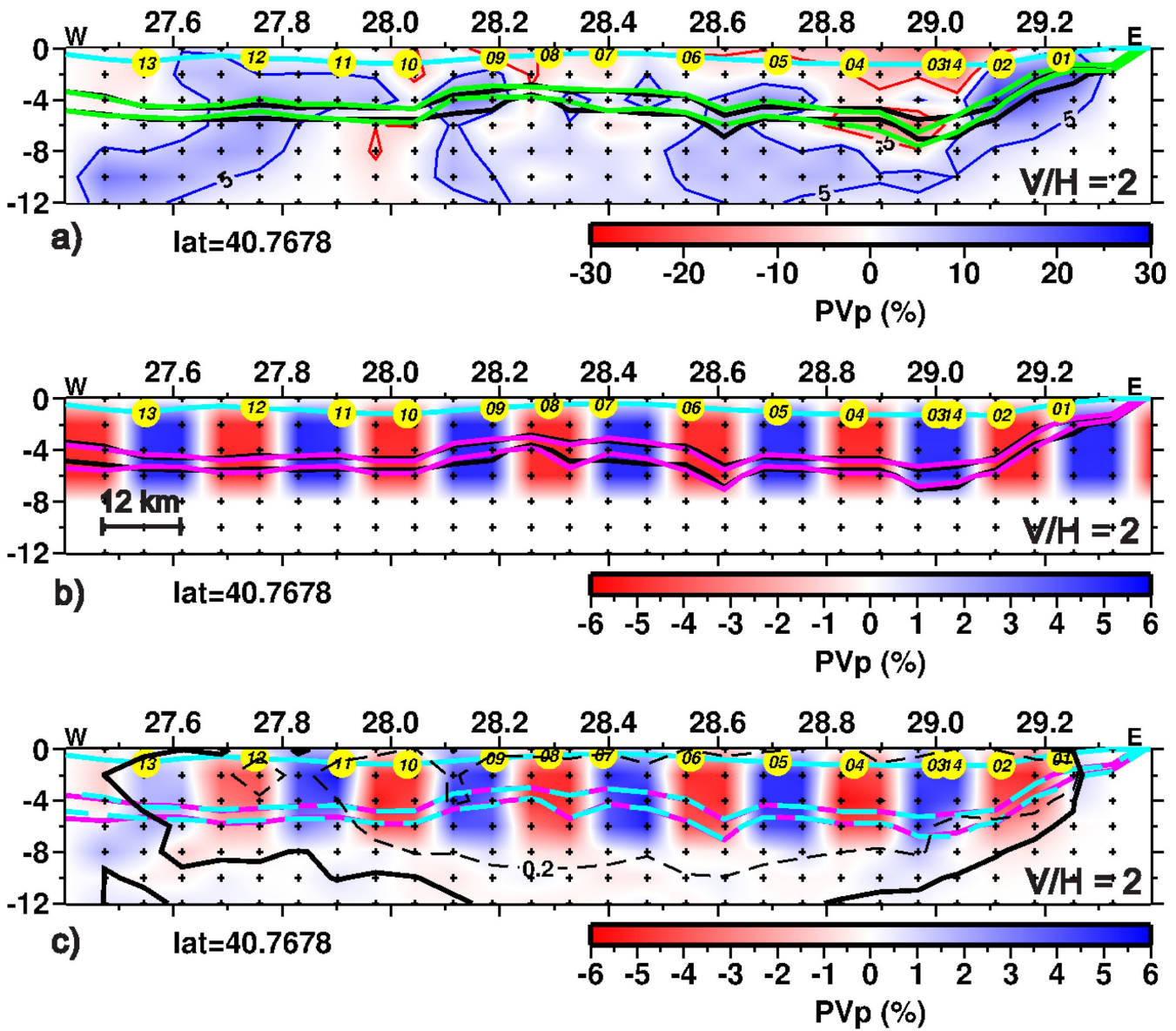
Figure 6. (a) The percentage velocity perturbation with respect to the 3-D initial model at the end of the inversion of the real data, along the same E–W cross-section as in the Fig. 4. Yellow circles are OBSs along the profile. The seafloor bathymetry is shown in blue line. Black contours are 4.2 (top) and 5.2 (bottom) km s^{-1} iso-velocity contours of the 3-D initial model, and green ones are the same iso-velocity contours obtained after the inversion (three iterations, damping 150). (b) The checkerboard pattern, which is injected to the 3-D initial model. It contains 12 km × 12 km × 6 km anomalies of ±5 per cent of amplitude. Notice that the colour scale is different form the one in the section a. Black contours are 4.2 (top) and 5.2 (bottom) km s^{-1} iso-velocity contours of the 3-D initial model, and pink contours are the same iso-velocity contours obtained by perturbing the 3-D initial model with the checkerboard pattern. (c) The result of the synthetic inversion. Pink contours are the same as in the section b and the dashed blue contours are the 4.2 (top) and 5.2 (bottom) km s^{-1} iso-velocity contours obtained after the synthetic inversion (three iterations, damping 150). Dashed and bold black contours surround good (RDE = 0.2) and acceptable (RDE = 0.05) resolution areas, respectively

corresponds to the NE boundary fault of the basin imaged by MCS (Fig. 8b). The 4.2 km s^{-1} iso-velocity contour is globally similar to the basement topography imaged by the MCS and this similarity confirms the reliability of the results of both methods. However, the 4.2 km s^{-1} iso-velocity contour appears less steep than the NE boundary fault imaged on the MCS. The difference between two images is due to the tomographic grid parametrization. The present grid undersamples in depth and in map this so sharp vertical (the shallow sea-bottom and the outcropping basement case) and lateral (the nearly vertical fault case) change in structural units. This aspect must be considered during the interpretation of the results.

The southern border of the Çınarcık Basin is also marked by a lateral velocity contrast. Along the superimposed section (Fig. 8b) the 4.2 km s^{-1} iso-velocity contour remains nearly 1s twt deeper than the outcropping basement observed on the MCS profile (Fig. 8b). When the letter is deeper than 1 km depth, its topography is perfectly retrieved as seen on the profile SM 8 (Fig. 8d), which samples the western part of this basement high.

Within the Çınarcık Basin low velocities corresponding to the sediments reach at least down to 4 km depth (Fig. 8a). The northward dipping shallow iso-velocity contours retrieved by the tomography are consistent with the northward fanning of the sedimentary
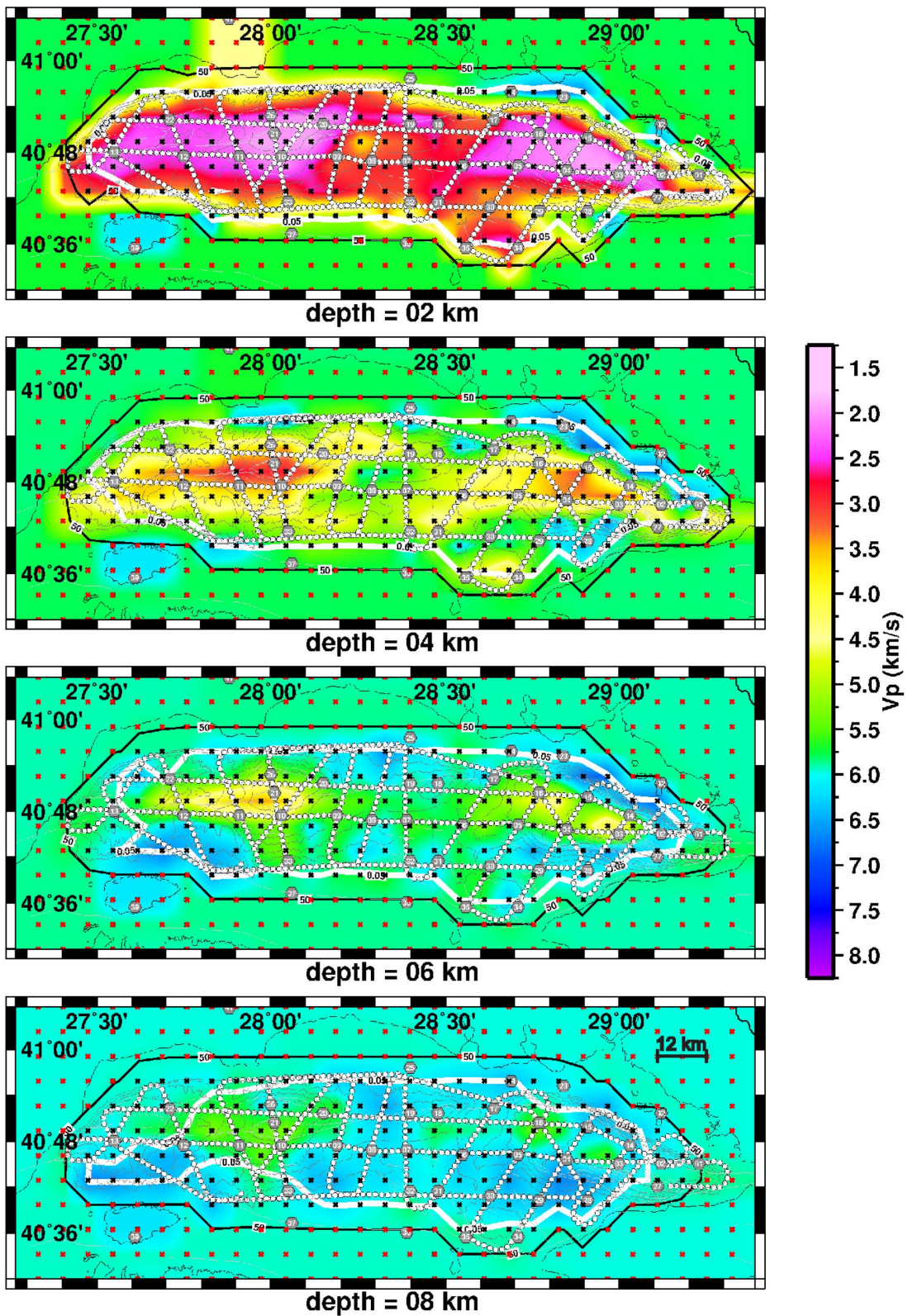
Figure 7. The map view at 2, 4, 6 and 8 km depths of the inversion results with the 3-D initial model. Grey hexagons are receivers (OBSs and land stations) of the survey. The white points are the considered shots. The white contour (RDE = 0.05) surrounds the well-resolved nodes identified by the checkerboard test. The black contour (DWS = 50) surrounds the nodes, which have been inverted during the inversion. The black crosses are the inverted nodes whereas the red ones are the fixed ones.
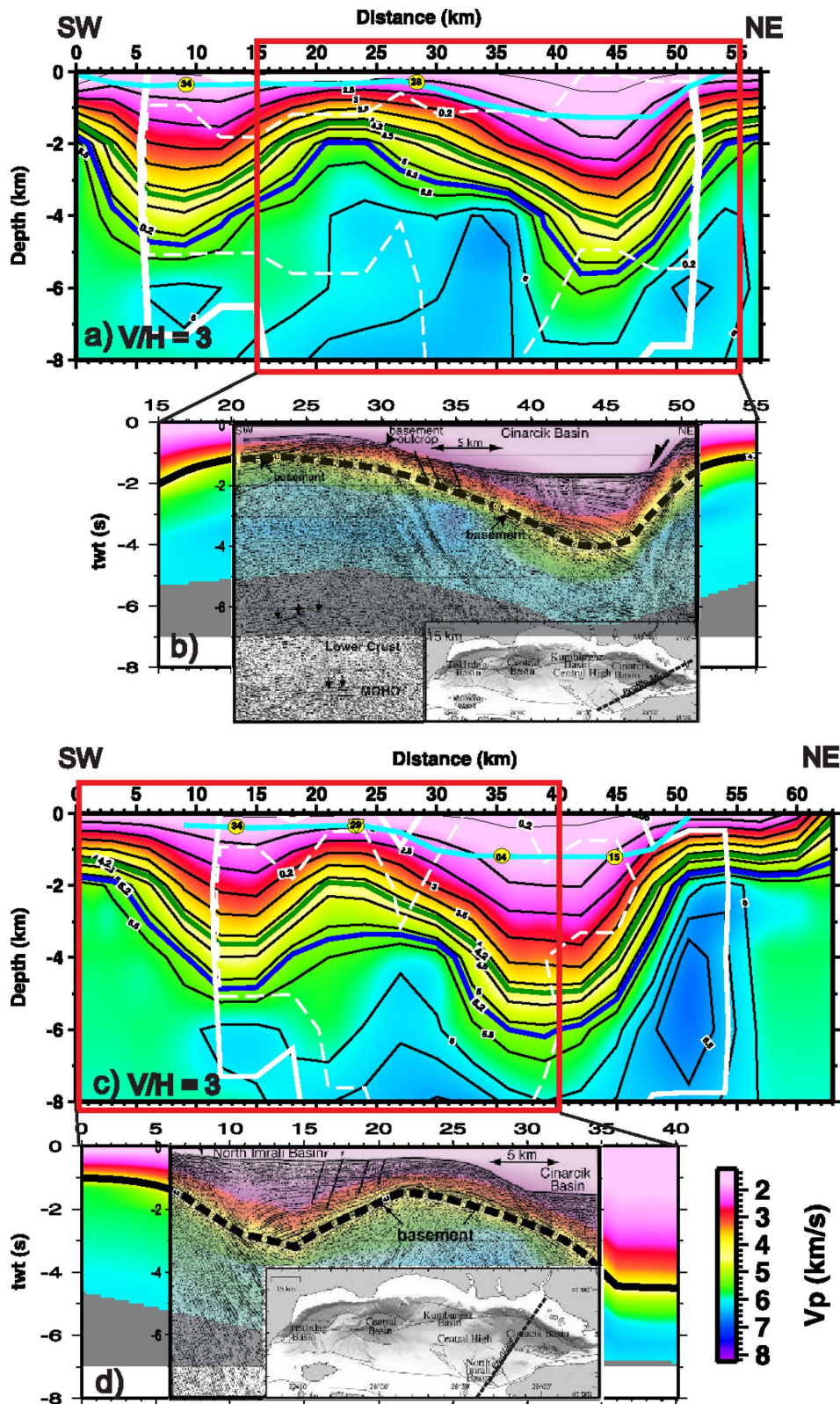
Figure 8. (a) The tomographic result along the SM36. Yellow circles represent the OBSs along this profile. The seafloor bathymetry is represented in blue. 4.2 (in green) and 5.2 km s^{-1} (in blue) contours are used as visual guides for pre-kinematic and crystalline basements, respectively. Solid (RDE = 0.05) and dashed (RDE = 0.2) white contours represent the areas with fairly and good resolution, respectively. Vertical exaggeration: 3. The red frame shows the location of the tomographic cross-section in (b). (b) The tomographic section SM36 transformed in twt and superimposed on the corresponding MCS section (Laigle *et al.* 2008). The black contour represents the 4.2 km s^{-1} iso-velocity contour in twt. The inset shows the location of the SM36. The solid line is the location of the MCS line and the dashed line is the location of the tomographic cross-section in (a). (c) The tomographic inversion result along the SM8 T. (d) Tomographic section SM8 transformed in twt and superimposed on the corresponding MCS section (Laigle *et al.* 2008).

deposits imaged on MCS (Fig. 8b). This suggests that sediments deposited above a subsiding basement are controlled by the NE boundary fault of the Çınarcık Basin, which has a normal component. It may still be active but the images do not allow to confirm or to reject this aspect.

The N35°E oriented SM8 cuts the eastern part of the North Imralı Basin to the south and the central part of the Çınarcık Basin to the north. The 4.2 km s^{-1} iso-velocity contour reaches down 3.75 km depth beneath the North Imralı Basin and to 5 km depth beneath the central part of the Çınarcık Basin (Fig. 8c). On the time section superimposed to SM8 (Fig. 8d), the 4.2 km s^{-1} iso-velocity contour fits clearly the basement topography retrieved by the MCS all along the profile. This profiles confirms that the sedimentary thickness within the North Imralı Basin is on the same order of magnitude than for the Çınarcık Basin. Within the North Imralı Basin, the southward dipping shallow iso-velocity contours are consistent with the southward fanning of the sedimentary deposits imaged by the MCS. These two tomographic sections (SM36 and SM8) confirm the opposite dipping of the basement under the Çınarcık and the North Imralı basins as proposed by Laigle *et al.* (2008) from the study of MCS profiles.

5.4 The margin of the southern continental shelf and the central high

5.4.1 The margin of the southern continental shelf

Along the southernmost E–W regional profile sampling the southern margin of the NMT (seafloor depth ∼100 m) tomographic and WARR modelling results show a thin sedimentary cover and a succession of basement depth variations of 1 km, although the second retrieves the basement depth systematically 1 km shallower (Fig. 9a). A similar shift is also observed at depth for the crystalline basement. The misfits between the observed and calculated travel times of both methods are in the same order and do not exceed 0.2 s. The quality estimators indicate good resolution at the eastern and westernmost part of this tomographic cross-section even if this profile remains at the limit of the zone covered by the network. The observed basement depth difference between two methods may be due to the consideration of the 3-D ray propagation in the 3-D tomography or to the consideration of secondary arrivals in the WARR modelling. It can also be due to the interpolation between the grid nodes as in the 'shallow sea bottom and outcropping basement' case.

For the eastern third of the profile, the 4.2 km s^{-1} iso-velocity contour fits very well the MCS-retrieved basement reflector which deepens smoothly from 1.2 s twt at the easternmost part of the profile, to 2.8 s twt towards the central part of the profile (Fig. 9b). At the western part of the profile, contrarily to WARR modelling, the MCS-retrieved pre-kinematic basement remains deeper than the iso-velocity contour of 4.2 km s^{-1}. At the westernmost part of the profile the 4.2 km s^{-1} iso-velocity contour fits the shallower part of the detachment imaged by Laigle *et al.* (2008) and Bécel *et al.* (2009). This reflector which is visible down to 7 s in twt on the MCS profile has been interpreted as an intracrustal detachment by the authors because of its larger dip than the expected dips for the lithological boundaries and its reverse polarity on the seismic image. The information concerning the shallower part of this detachment was included to the 3-D initial model and the inversion does not modify this *a priori* information. Over the detachment, the MCS profile reflects a succession of tilted basement blocks. Contrarily to

WARR modelling, the MCS retrieved basement is deeper than the tomographic one. However, due to the small scale of tilted basement blocks, the 3-D tomography onto 6 km × 6 km inversion grid does not fully capture this complex lateral heterogeneity.

5.4.2 Central high

We compared the tomographic result with the N–S cross-section, OBS-line 5 and with the corresponding MCS profile, SM5 which sample the western part of the Kumburgaz Basin, the Central High and the southern shelf (Fig. 10). The basement expression of the Central High is located between two basement depressions and it rises up to 3 km depth along this profile. The crest position of the basement is not located beneath the bathymetric Central High but it is 5 km northward, at the latitude 40° 50'. The two basement depressions appear as topographic variations of 1 km occurring from one node to another. The crystalline basement topography is also affected by these variations. The northern depression is approximately located beneath the seafloor trace of the NAF and corresponds to its basement expression where, pre-kinematic and crystalline basements reach down to 3.75 and 5 km, respectively. The velocity contrast between the northern shelf and the northern depression indicates that the NAF has or have had an extensional component at this location. Beneath the southern depression, which corresponds to the western continuation of the Çınarcık Basin (Carton *et al.* 2007; Bécel *et al.* 2010), the pre-kinematic and the crystalline basements are slightly shallower than beneath the northern one.

Even if the WARR modelling results have been used as *a priori* information into the 3-D initial model, the 3-D tomography retrieves a smoother pre-kinematic basement topography than the initial one. The quality estimators indicate good resolution at this part of the study volume. The retrieved smoothed topography is thus due to small wavelength and high amplitude lateral velocity heterogeneity of the region sampled by this profile. A test inversion with a shifted grid has shown that the small wavelength heterogeneity cannot be fully represented by the actual inversion grid and that the places of the grid nodes have an influence on the retrieved anomalies. Nevertheless, the comparison of the tomographic result with the SM5 (Fig. 10b) shows that the image retrieved by the tomography is reliable. It provides a smoother version of the real tomography.

5.5 The western third of the Marmara Sea: the Central and the Tekirdağ basins

5.5.1 The Central basin

On the tomographic and WARR modelling results along N–S oriented OBS-line three across the deep Central Basin, northern and southern basin borders appear asymmetrical (Fig. 11). However two methods retrieve different basement topographies. WARR modelling retrieves a flat-bottomed basin at of 8 km length at 7 km depth whereas the tomography retrieves a basin bottom at 6 km depth with basin borders separated from each other by a distance of 3 km at this depth.

The time section superimposed on the corresponding seismic line, SM46 confirms that the 3-D tomography captured accurately the places of the basin bounding faults (F1, F2) as lateral velocity contrasts (Fig. 11d). The 4.2 km s^{-1} iso-velocity contour is affected by these faults suggesting that they reach down to the pre-kinematic basement. In the central part of this profile (at the CDP 3900 on Fig. 11d), the tomographic result indicate a basement depression
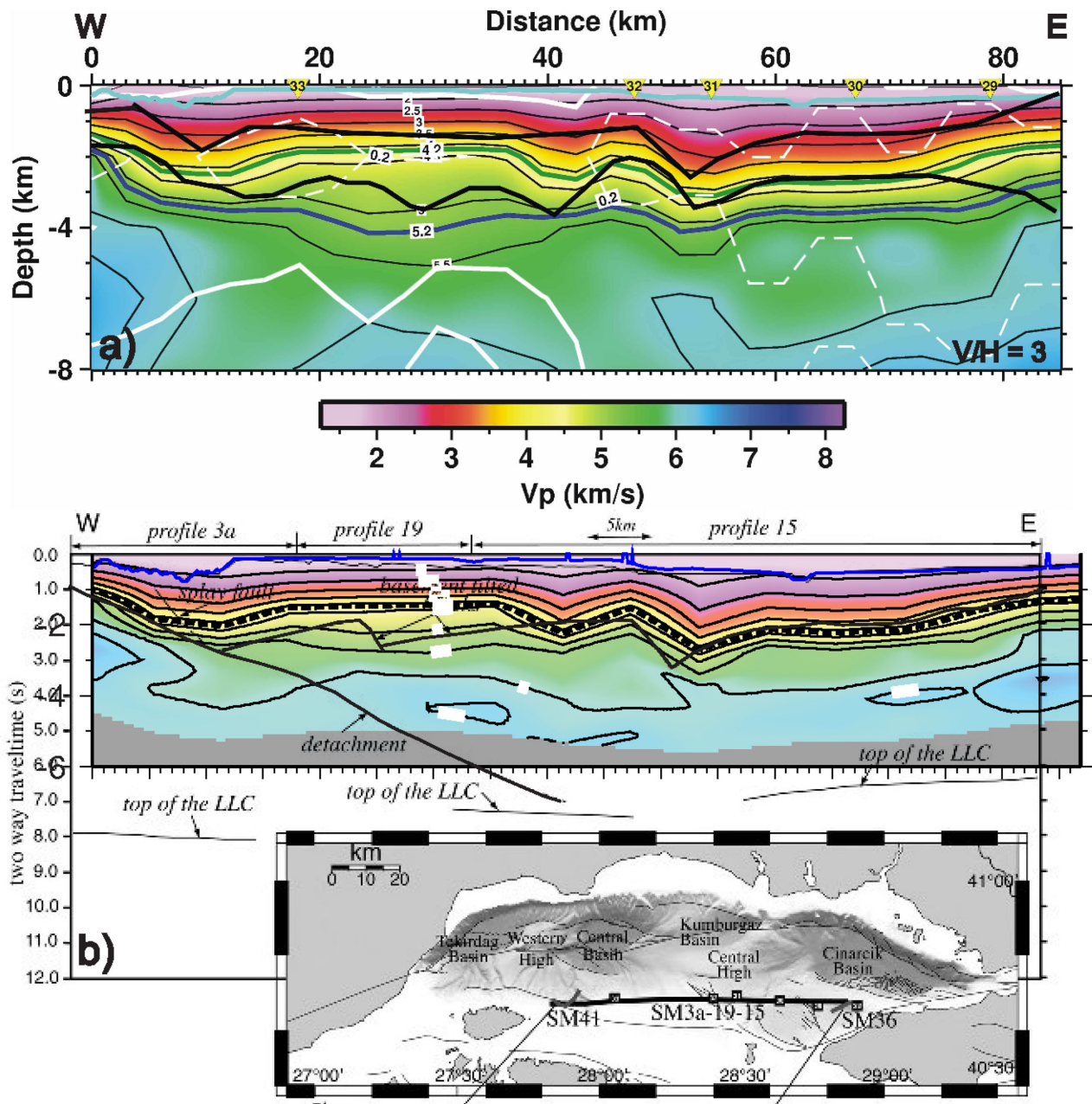
Figure 9. (a) The 3-D tomographic result along southern E-W profile of 85 km lying on the margin of the southern continental shelf. Yellow triangles represent OBSs along the profile. The seafloor bathymetry is represented in blue line. $4.2 \, \mathrm{km \, s^{-1}}$ (in green) and $5.2 \, \mathrm{km \, s^{-1}}$ (in blue) contours are used as visual guides for pre-kinematic and crystalline basements, respectively. Solid and dashed white contours represent areas of fairly and good resolution, respectively. Two black lines are pre-kinematic (top) and crystalline (bottom) basements resulting from the WARR modelling (Bécel *et al.* 2009) Vertical exaggeration: 3. (b) Same profile transformed in two way travel time and superimposed on the corresponding interpretation of the MCS profile (Laigle *et al.* 2008). The $4.2 \, \mathrm{km \, s^{-1}}$ iso-velocity contour transformed in twt is represented in dashed black contour. Inset shows the location of the cross-section.

which is located at the prolongation in depth of the MCS retrieved intra basin fault F4. This suggests that F4 affects also the basement. At the southern half of the profile (between the CDP 2900 and 3500), the northward dipping shallow iso-velocity contours are consistent with the dip of sedimentary depocentres imaged by the MCS. The MCS-identified fault F5 which interrupts the continuous stratification between F2 and F4 is not captured by the 3-D tomography due to its small wave length, due to the fact that it does not affect the basement or it does not have significant vertical throw. At the northern part of the profile, between the F1 and F3, shallower iso-velocity contours are consistent with the southward dipping of

sedimentary deposits imaged by MCS. However the tectonized region corresponding to the fault F3, between the CDP 4500 and 4000, is not observed on the tomographic image neither as a basement depression nor as northward dipping of shallow iso-velocity contours.

5.5.2 The Tekirdağ basin

On the map view of the inversion results Tekirdağ Basin appears with sedimentary velocities down to 4 km depth at its western part, and down to 6 km depth at its eastern part. On the seafloor
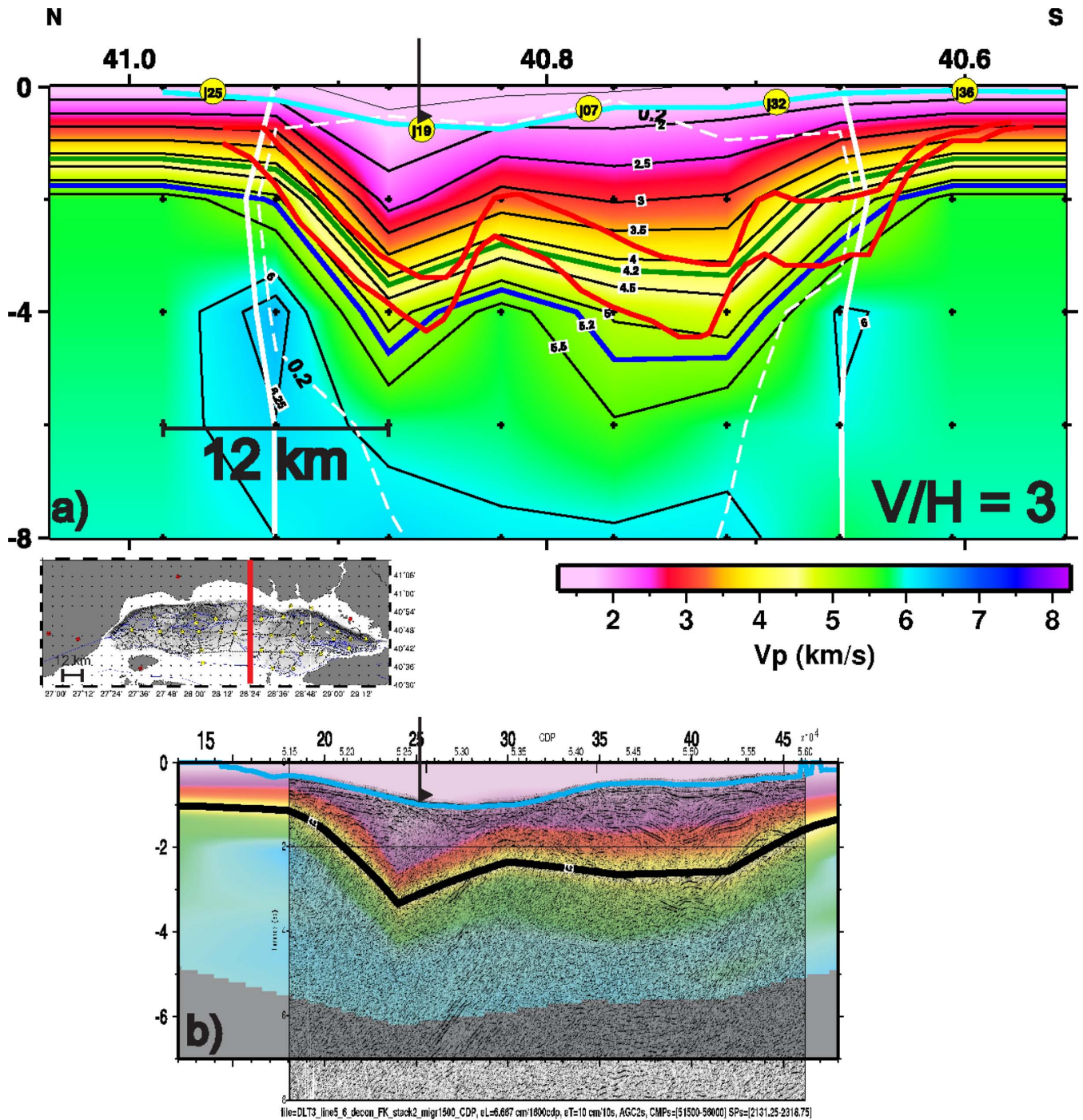
Figure 10. The 3-D tomographic result along N–E OBS-line five which cuts across the northern shelf, the western part of the Kumburgaz basin, the Central High and the southern shelf. Yellow circles represent OBSs along the profile. The seafloor bathymetry is represented in blue line. 4.2 km s^{-1} (in green) and 5.2 km s^{-1} (in blue) contours are used as visual guides for pre-kinematic and crystalline basements, respectively. Solid and dashed white contours represent areas with fairly and good resolution, respectively. Two red contours are pre-kinematic (top) and crystalline (bottom) basements resulting from the WARR modelling (Bécel *et al.* 2009.)

topography the Tekirdağ and the Central basins (seafloor depth >1200 m) appear separated by the NE oriented Western High (seafloor depth <500 m). However, the E–W profile which cuts the deeper part of the three basins shows that in depth the Tekirdağ Basin is linked with the Central Basin (Fig. 12) forming a large basement depression of 66 km and there is no evidence of a basement high corresponding to the Western High which is only observed on the seafloor topography.

6 DISCUSSIONS

6.1 The map of the pre-kinematic basement topography and the sedimentary thickness

Up to now the only 3-D view of the Marmara Sea was the high-resolution bathymetric map of Le Pichon *et al.* (2001) and Armijo *et al.* (2002). The present 3-D tomographic inversion allowed us to
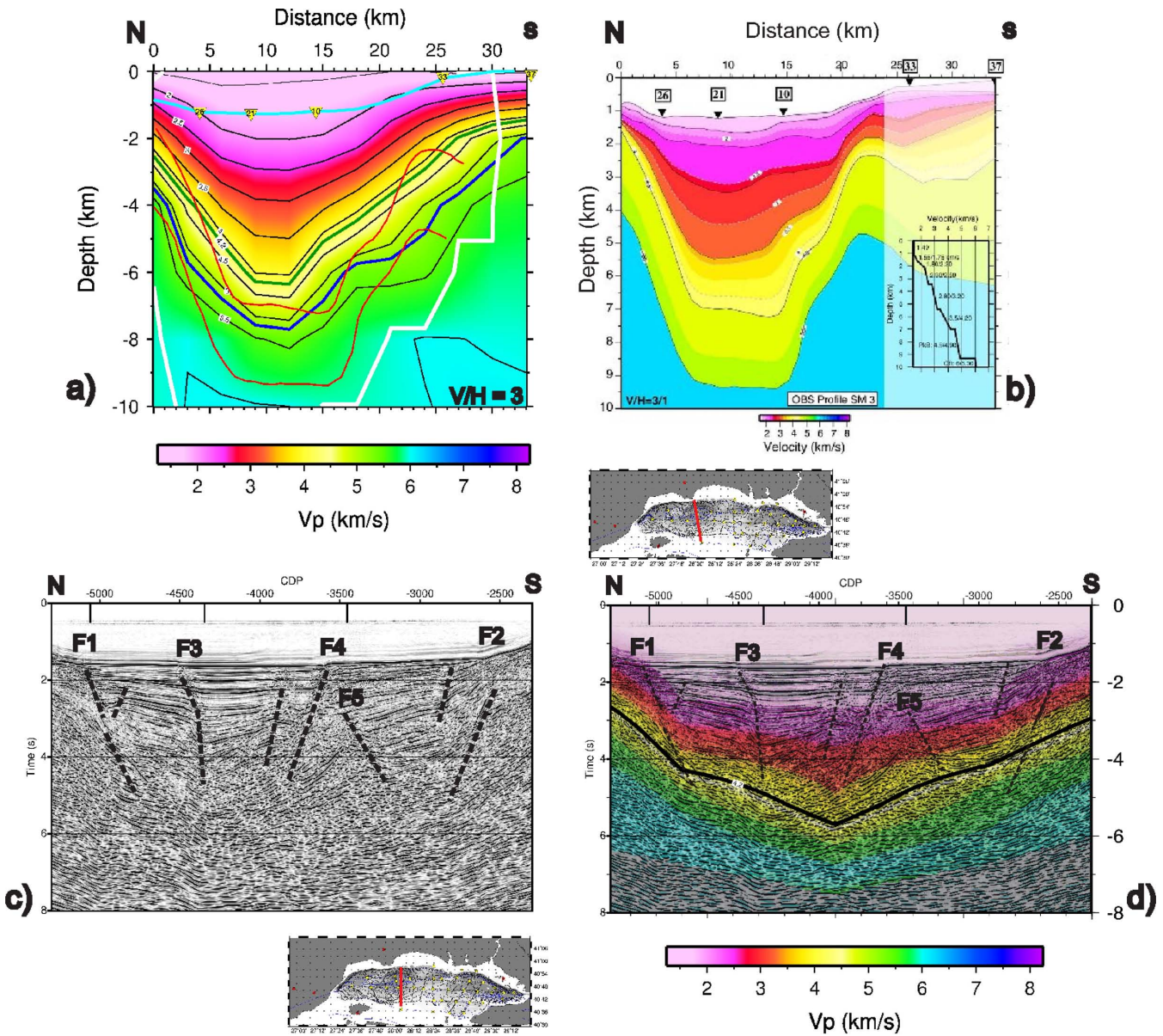
Figure 11. (a) The tomographic inversion result along the N-S OBS-line 3, which cuts across the Central Basin. Yellow triangles represent in-line OBSs. The seafloor bathymetry is represented in blue line. 4.2 km s^{-1} (in green) and 5.2 km s^{-1} (in blue) contours are used as visual guides for pre-kinematic and crystalline basements, respectively. Solid white contour represents the areas with fairly resolution. Topographies of pre-kinematic (top) and crystalline (bottom) basements retrieved by WARR modelling are exported on the tomographic results, in red lines. (b) 2-D wide-angle reflection refraction modelling result along the same profile after Bécel *et al.* 2010. The inset shows the location of the cross-section. (c) The corresponding MCS line SM46 in two way travel time (twt). The inset shows the location of the profile 46. (d) The tomographic result along the same profile, transformed in twt and superimposed on the MCS section.

derive the 3-D *Vp* heterogeneity of the Marmara sea's supracrustal part and to obtain the first fully 3-D view of the second major interface beneath the Marmara Sea that is the pre-kinematic basement (Fig. 13a).

The basement map is obtained by extracting the iso-velocity surface of 4.2 km s^{-1} from the 3-D *Vp* heterogeneity model. Hence it has the same resolution as the 3-D *Vp* heterogeneity model, which is defined on the grid nodes with 6 km interval in the horizontal directions and 2 km in the vertical direction. The basement map gives insight about basement expressions of the Marmara Sea's bathymetric elements. Before any interpretation, orientations and dips of these elements must be analysed carefully. The fact that the inversion provides a smoothed view of the real basement topography and that places of grid nodes have an

impact on the locations of retrieved anomalies must be keep in mind.

The map of the pre-kinematic basement topography together with the high-resolution bathymetric map allowed us also to derive the map of the sedimentary thickness of the NMT. The seafloor depth is subtracted from the depth of the pre-kinematic basement at the locations of the inversion grid nodes. Sedimentary thickness values are interpolated linearly between grid nodes. The obtained map of the sedimentary thickness has similar resolution as the map of the basement topography. Carton *et al.* (2007) have provided a similar map of the sedimentary thickness for the Çınarcık Basin by studying very densely spaced MCS lines of the second leg of the SEISMARMARA survey. The present sedimentary thickness map has a lower resolution. However, the refraction data from profiles
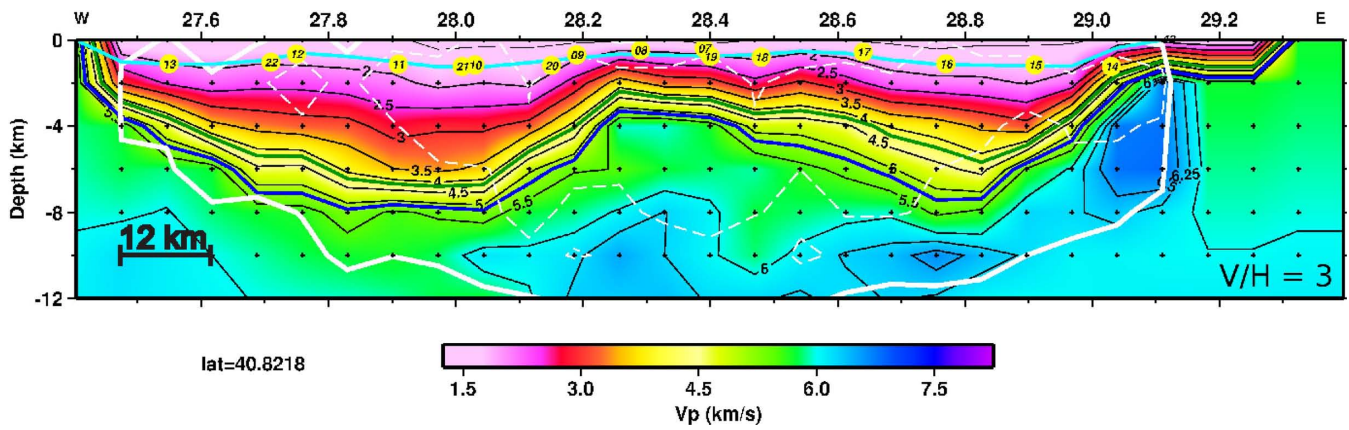
Figure 12. The E–W tomographic section at the latitude 40.8218° cutting across the deeper part of the basins. The yellow triangles represent the OBSs along this profile. The seafloor bathymetry is represented in blue line. 4.2 km s^{-1} (in green) and 5.2 km s^{-1} (in blue) contours are used as visual guides for pre-kinematic and crystalline basements, respectively. Solid white contour represents the areas with fairly resolution.
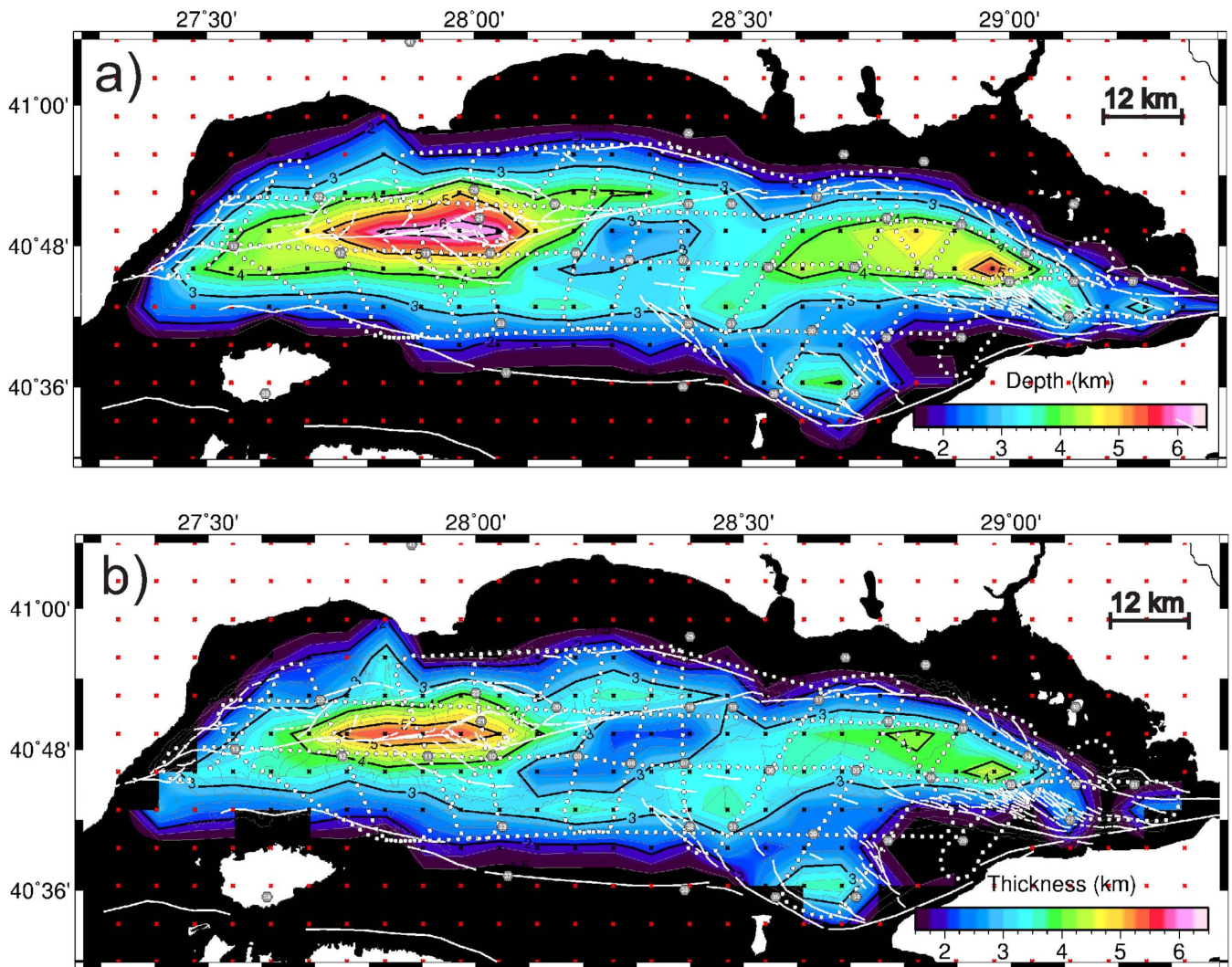

Figure 13. (a) Map of the pre-kinematic basement topography. Submarine fault scarps after Armijo *et al.* 2002 are represented in white. Black crosses are inverted nodes and red ones are fixed ones. Receivers (OBSs and land stations) are represented in grey hexagons. (b) Map of the sedimentary thickness obtained by subtracting the seafloor depth from the basement depth at grid node positions.

shot with the larger source and with a larger shot interval offer larger penetration in depth which is necessary to approach the sedimentary thickness by retrieving the basement depth continuously overall NMT, even beneath the deep sedimentary basins.

6.2 Two distinct sedimentary deposits within the Çınarcık basin

The Çınarcık Basin appears with a maximum sedimentary thickness of 4.5 km (Fig. 13b) which is consistent with the previous observation of Okay *et al.* (2000) who proposed 4 km of sedimentary thickness, likely to consist of Pliocene–Quaternary syn-kinematic sediments. Within the Çınarcık Basin we observed two distinct zones where the sedimentary thickness reaches up to 4.5 km. One of them is located at the widest part of the sea-bottom expression of the Çınarcık Basin, southwest of the bend of the northern escarpment. The second one is eastwards, at the hanging wall of the southern bounding fault, just north of the en echelon structure imaged at the seafloor morphology (Fig. 13). Carton *et al.* (2007) have observed the first sedimentary accumulation as being the deepest part of the basin, with a sedimentary thickness of 5–6 km by considering an average velocity of 2–2.5 km s^{-1} for the sedimentary cover. Based on the sedimentary thickness getting thinner eastwards, authors have proposed an eastward migration over time of this depocentre that they considered as the oldest part of the basin. Within the second depocentre Carton *et al.* (2007) observed a sedimentary thickness of 4.5 km, which is consistent with the present results. The sedimentary thickness difference observed within the first depocentre could be explained by the limited confidence on reflection profiles at the western and deeper part of the Çınarcık Basin (Carton *et al.* 2007). Alternatively, if the thickest part of this depocentre is not located near by a grid node, the tomography may retrieve a smoothed basement topography which would yield a lower sedimentary thickness at this location. The subsidence and deformation history on a large-scale lower structure comprising the Çınarcık and the North Imrali basins may form these two distinct depocentres within the Çınarcık Basin.

6.3 The transition region between the Çınarcık and the Central basins

In the region comprising the eastern tip of the Central Basin, the Central High, the Kumburgaz Basin and the western tip of the Çınarcık Basin, that we called transition region, the seafloor topography is not mirrored by the basement topography. We observed a NE–SW oriented basement high which rises up to 3 km depth on a 18 km large zone that is located between two deep basins (Fig. 13a). The crest position of this basement high is approximately 10 km northwestward than the bathymetric crest of the Central High. To the west, it appears interrupted by the eastern border of the Central Basin of N40°E orientation where the basement deepens 1 km abruptly, within 6 km distance (Fig. 13). To the north, it is interrupted by a narrow basement depression of 4 km depth, which is also seen on the OBS-line and SM5 (Fig. 10). This E–W oriented northern basement depression follows approximately the seafloor trace of the NAF of N80°E orientation. An inversion test carried out with a rotated inversion grid confirmed that the E–W orientation of this basement depression is not imposed by the orientation of inversion grid nodes although places of grid nodes affect slightly the places of retrieved anomalies. This depression appears to be linked by the Central Basin to the west and it stops before to reach

beneath the bathymetric expression of the Kumburgaz Basin to the east. There is no tomographic evidence of a basement depression beneath the bathymetric expression of the Kumburgaz Basin. This can be due to the small size of this basin, which might be too small with respect to the node interval. The basement expression of the Central High is limited by the western part of the Çınarcık Basin to the east. Here, the basement deepens more gradually with respect to the western part.

An important new finding is the second narrow basement depression, which is observed southwestward of the Central High. This nearly 4 km depth E–W oriented depression has a similar from as the northern one, which corresponds to the basement expression of the NAF. This southern narrow depression may be related with the normal faults which limit the tilted basement blocks located over the intracrustal detachment which have been imaged on the southern E–W MCS profile by Laigle *et al.* (2008) (Fig. 9b).

These tilted basement blocks have also been imaged along a set of transect MCS profiles sampling the zone from the western part of the southern shelf, to the southern parts of the Western High and the Central Basin as southward dipping reflections (Laigle *et al.* 2008; Bécel *et al.* 2009). On the map of the basement topography (Fig. 13a) or on the tomographic cross-sections sampling this zone (Figs 9 and 11), there is no evidence of such tilted basement blocks. Instead, the basement depth increases continuously from the southern border of the NMT to the deeper part of the Central Basin. Bécel *et al.* (2009) have inferred a block size of 17 km and a block height of 1 km by analysing crest position of the western block (called block a) along a set of MCS profiles with different azimuths. The absence of these tilted blocks on the map of the basement topography may be due to their small height, which is smaller than the vertical node interval of the grid (2 km).

6.4 The Western third of the Marmara sea

At the deeper part of the Central Basin, the map of the basement topography indicates a basement depth of more than 6 km and a maximum sedimentary thickness of 5.5 km. On the seafloor topography this basin appears to be limited to the west by the Western High and to the east by the Central High. However the map of the basement topography has major differences with the seafloor topography. Beneath the bathymetric expression of the Western High there is no evidence of a corresponding basement high. But instead, the basement appears at 6 km depth, as deep as beneath the Central Basin itself. The absence of basement high related to the Western High suggests that the western high is a relief formed by the sediments. The Tekirdağ and the Central Basins appear thus linked, forming one large basement depression whose deepest part is located beneath the Central Basin and Western High. This suggests that both basins developed under the same mechanism. The orientation of this elongated rhomboidal basement depression of nearly 60 km length and 20 km width is N80°E, similar to the orientation of the seafloor trace of the 'Main Marmara Fault' proposed by Le Pichon *et al.* 2001. The northeastern corner of this depression is linked to the narrow basement depression which cuts across the Central High and which is also located beneath the seafloor trace of NAF.

6.5 *A priori* information for further geophysical applications

The obtained upper-crustal *Vp* heterogeneity model of the Marmara Sea provides a realistic initial model for the LET. The

limited number of earthquakes recorded by the SEISMARMARA network did not allow us to derive the supracrustal heterogeneity of the Marmara Sea by LET. Occurring at depths within brittle part of the crust, earthquakes do not usually provide enough cross-sampling to constrain the very heterogeneous upper-crustal part. The controlled source data obtained by air-gun shots at the sea level provide a better cross-sampling at the upper part of the crust. Furthermore, the controlled source inversion includes less unknown parameter than LET studies and it offers a more homogeneous resolution distribution. In a region where the thickness of the sedimentary cover varies by several kilometres, the use of 3-D upper-crustal Vp heterogeneity model obtained by this controlled source inversion, as an initial model in LET may improve the earthquake relocations. The code Simulps used for the controlled source inversion allows now to include the P and S arrivals of local earthquakes recorded by the network into the inverted data set for the joint relocation of the earthquakes and inversion for Vp and Vp/Vs structure with the same code and with the same inversion parameters.

The resolution of the 3-D Vp heterogeneity is achieved for the whole thickness of the sedimentary domain down to the top of the crystalline crust. The final Vp pattern allowed us to obtain the first 3-D view of the pre-kinematic basement beneath the Marmara Sea. Up to now, owing to the absence of such information, the geomechanical modelling studies did not take into account the variations of the seismogenic zone along the active faults of the Marmara Sea. However, the present map of the basement topography has shown that between the deep sedimentary basins and the basins borders with outcropping basement, the basement depth vary sometimes more than 5 km. This implies variations of the same order into the size of the seismogenic zone along the active faults. The present map of the basement topography offers the possibility to take into account these large variations into the geomechanical modelling for geohazard estimations.

7 CONCLUSIONS

Here we obtained the 3-D Vp velocity structure beneath the North Marmara Trough by a controlled source first arrival time tomography. Several 1-D initial models were first tested in order to have a hint of the physically possible solutions. All tested 1-D initial models yield very high *a priori* residuals (S1) and test inversions with these models yield large reduction in the data variance. Regardless to the 1-D initial model, the main structural elements of the NMT were retrieved beneath the zone covered by the shot-and receiver network. However, 1-D models produced unrealistic velocities in low-resolution areas. Moreover, due to the very high velocity perturbations (>30 per cent) with respect to 1-D initial models, some leakage of up to 15 per cent were observed at the under-resolved areas showing that 1-D initial models are not appropriate to represent the complex upper-crustal structure of the Marmara Sea. Therefore, a 3-D initial model was built up by introducing the available *a priori* information about the topographies of main interfaces that are the seafloor bathymetry, the pre-kinematic and the crystalline basements and the Moho. The inversion results with this 3-D initial model were presented after the validation of the reliability of retrieved anomalies by checker-board tests (Figs 6 and S4), and compared to the results obtained with other methods (wide angle and multichannel seismic results).

The final 3-D Vp model indicates velocity contrasts occurring between two nodes (in 6 km distance) at the borders of NMT. Within the three deep basins of the Marmara Sea (seafloor depth >1200 m),

sedimentary velocities (1.8–4.2 km s^{-1}) are observed down to 6 km depth.

Beneath the North Imrali Basin located on the southern platform (seafloor depth ~400 m), the basement depth appears as 4 km suggesting that the sedimentary thickness within this basin is comparable to the ones of its northern neighbours. The North Imrali and the Çınarcık basins are separated by an E-W basement high, which rises up to 3 km at its western part and crops out at its eastern part. Within the Çınarcık Basin, the pre-kinematic basement depth locally reaches up to 5 km and two distinct depocentres are imaged with up to thicknesses of 4 km.

The basement expression of the Central High rises up to 3 km depth. Its crest position is offset by 10 km northwestward relatively to the bathymetric crest. To the north, the Central High is interrupted by a N80°E oriented narrow basement depression of 4 km depth corresponding to the basement expression of NAF. This basement depression stops before to reach the Kumburgaz Basin. Most probably due to its small wavelength with respect to the 6 km $\times$ 6 km $\times$ 2 km inversion grid, there is no tomographic evidence of a basement depression beneath the Kumburgaz Basin. To the south, the basement expression of the Central High is interrupted by a second narrow basement depression of where the basement depth reach down to 4 km depth. This depression may form the limit of the tilted basement blocks documented in MCS data, at the southern limit of the NMT. However, there is no tomographic evidence for these tilted basement blocks, which do not necessarily correspond to a unique iso-velocity contour. The tilted blocks were most probably imaged thanks to their impedance contrast on the MCS profile.

Contrarily to Central High, no basement high was found beneath the bathymetric expression of Western High. The Tekirdag and the Cantral Basins appears thus linked, forming one large basement depression of rhomboidal shape where the basement depth reaches down to 6 km below the seafloor.

The final 3-D Vp heterogeneity model provides a realistic initial model for future LET studies in the Sea of Marmara. The use of a 3-D upper-crustal Vp heterogeneity model in LET studies, might improve earthquake locations by taking into account the sedimentary thicknesses not only locally beneath the OBSs, but in three dimensions. Together with the Moho depth obtained by the wide angle study (Bécel *et al.* 2010), the basement topography presented here offers the possibility to consider locking depth variations in future geomechanical modelling for geohazard estimation. As for the map of the sedimentary thickness, together with the active faults imaged by the MCS, it might bring new information about the present activity and evolution of the Marmara Sea's features.

REFERENCES

Aksu, A.E., Hiscott, R.N. & Yasar, D., 1999. Oscillating quaternary water levels of the Marmara Sea and vigorous outflow into the Aegean Sea from the Marmara Sea-Black Sea drainage corridor, *Mar. Geol.,* **153,** 275–302.

Armijo, R., Meyer, B., Navarro, S., King, G. & Barka, A., 2002. Asymmetric slip partitioning in the Sea of Marmara pull-apart : a clue to propagation processes of the North Anatolian Fault, *Terra Nova,* **14,** 80–86.

Armijo, R. & the Marmarascarps Cruise Party, 2003. Young earthquake breaks in the Sea of Marmara floor: a possible underwater extension of the 1912 earthquake rupture? AGU-EGS-EUG Joint Meeting, Nice, France (6–11 April 2003).

Avedik, F., Nicolich, R., Hirn, A., Maltezou, F., Mc Bride, J., Cernobori, L. & the STREAMERS PROFILES GROUP, 1995. Appraisal of a new high-energy, low frequency seismic pulse generating method on a deep seismic reflection profile in the Central Mediterranean Sea, *First Break,* **13,** 277–290.

Avedik, F., Hirn, A., Renard, V., Nicolich, R., Olivet, J.L. & Sachpazi, M., 1996. "Single-bubble" marine source offers new perspectives for lithospheric exploration, *Tectonophysics,* **267,** 57–71.

Barka, A.A., 1996. Slip distribution along the North Anatolian fault associated with large earthquakes of the period 1939–1967, *Bull. seismol. Soc. Am.,* **86,** 1238–1254.

Bécel, A. *et al.*, 2009. Moho, crustal architecture and deep deformation under the North Marmara Trough, from the Seismarmara Leg1 offshore-onshore reflection-refraction survey, *Tectonophysics,* **467,** 1–21.

Bécel, A., 2006. Structure Sismique de la Faille Nord Anatolienne en Mer de Marmara, *PhD thesis,* Institut de Physique du Globe de Paris.

Bécel, A. *et al.*, 2009. Moho, crustal architecture and deep deformation under the North Marmara Trough from the SEISMARMARA Leg-1 offshore-onshore reflection-refraction survey, *Tectonophysics,* **467,** 1–21.

Bécel, A., Laigle, M., de Voogd, B., Hirn, A., Taymaz, T., Yolsal-Cevikbilen, S. & Shimamura, H., 2010. North Marmara Trough architecture of basin infill, basement and faults, from PSDM reflection and OBS refraction seismics, *Tectonophysics,* **490,** 1–14.

Benz, H.M., Chouet, B.A., Dawson, P.B., Lahr, J.C., Page, R.A. & Hole, J.A., 1996. Three-dimensional P and S wave velocity structure of Redoubt Volcano, Alaska, *J. geophys. Res.,* **101**(4), 8111–8128.

Carton, H. *et al.*, 2007. Seismic imaging of the three-dimensional architecture of the Çınarcık Basin alongh the North Anatolian Fault, *J. geophys. Res.,* **112,** B06101, doi:10.1029/2006JB004548.

Demirbag, E., Rangin, C., Le Pichon, X. & Sengor, A.M.C., 2003. Investigation of the tectonics of the Main Marmara Fault by means of deep-towed seismic data, *Tectonophysics,* **361,** 1–19.

Dinc, A.N., Koulakov, I., Thorwart, M., Rabbel, W., Flueh, E.R., Arroyo, I., Taylor, W. & Alvarado, G., 2010. Local earthquake tomography of central

Costa Rica: transition from seamount to ridge subduction, *Geophys. J. Int.,* **183,** 286–302.

Eberhart-Phillips, D., 1990. Three-dimensional P- and S-velocity structure in the Coalinga region, California, *J. geophys. Res,* **95,** 15 343–15 363.

Eberhart-Phillips, D., 1993. Local earthquake tomography: earthquake source regions, in *Seismic Tomography – Theory and Practice,* pp. 613–643, eds Iyer, H.M. & Hirahara, K., Chapman and Hall, London.

Eberhart-Phillips, D. & Bannister, S., 2010. 3-D imaging of Marlborough, New Zealand, subducted plate and strike-slip fault systems, *J. geophys. Res,* **182,** 73–96.

Ergun, M. & Ozel, E., 1995. Structural relationship between the Sea of Marmara Basin and the North Anatolian Fault Zone, *Terra Nova,* **7,** 278–288.

Evans, J.R., Eberhart-Phillips, D. & Thurber, C.H., 1994. User's manual for SIMULPS12 for imaging *Vp* and *Vp/Vs*: a derivative of the Thurber tomographic inversion SIMUL3 for local earthquakes and explosions. *Open-File Rep,* U.S. Geol. Surv., U.S. Government Printing Office, 94–431.

Flerit, F., Armijo, R., King, G.C.P., Meyer, B. & Barka, A., 2003. Splip partitioning in the Sea of marmara pull-apart determined from GPS velocity vectors, *Geophys. J. Int.,* **154,** 1–7.

Grall, P. *et al.*, 2012. Heat flow in the Sea of Marmara Central Basin: possible implications for the tectonic evolution of the North Anatolian fault, *Geology,* **40**(1), 3–6.

Haslinger, F., 1998. Velocity structure, seismicity and seismotectonics of northwestern Greece between the gulf of Arta and Zakynthos, *PhD thesis,* ETH Zürich, Switzerland.

Haslinger, F. *et al.*, 1999. 3-D crustal structure from local earthquake tomography around the Golf of Arta (Ionian-region, NW Greece), *Tectonophysics,* **304,** 201–218.

Haslinger, F. & Kissling, E., 2001. Investigating the effects of 3-D ray tracing methods in local earthquake tomography, *Phys. Earth planet. Inter.,* **123,** 103–114.

Hergert, T. & Heidbach, O., 2010. Slip-rate variability and distributed deformation in the Marmara Sea fault system, *Nature Geoscience,* **3,** 132–135.

Hergert, T. & Heidbach, O., 2011. Geomechanical model of the Marmara Sea region – II. 3-D contemporary background stress field, *Geophys. J. Int.,* **185**(3), 1090–1102.

Hobro, J.W.D., 1999. Three-dimensional tomographic inversion of combined reflection and refraction seismic travel time data. *PhD thesis,* University of Cambridge, Cambridge.

Husen, S., Kissling, E. & Flueh, E., 2000. Local earthquake tomography of shallow subduction in north chile: a combined onshore and offshore study, *J. geophys. Res.,* **155,** 11–32.

Hobro, J., Sing, S. & Minshull, T., 1999. Three-dimensional tomographic inversion of combined reflection and refraction seismic travel time data, *Geophys. J. Int.,* **1,** 11–20.

Hobro, J. & Sing, S., 1999. Joint interface and velocity estimation in three dimensions (jive3d), *LITHOS Science Report*.

Imren, C., Le Pichon, X., Rangin, C., Demirbag, E., Ecevitoglu, B. & Görür, N., 2001. The North Anatolian Fault within the Sea of Marmara: a new interpretation based on multi-channel seismic and multi-beam bathymetry data.

Karabulut, H., Özalaybey, S., Taymaz, T., Aktar, M., Selvi, O. & Kocaoğlu, A., 2003. A tomographic image of the shallow crustal structure in the Eastern Marmara, *Geophys. Res. Lett.,* **30**(24), 2277–2280.

Kissling, E., Ellsworth, W.L., Eberhart-Phillips, D. & Kradolfer, U., 1994. Initial reference models in local earthquake tomography, *J. geophys. Res.,* **99**(B10), 19 635–19 646.

Koulakov, I. *et al.*, 2007. P and S velocity structure of the crust and the upper mantle beneath central Java from local tomography inversion, *J. geophys. Res.,* **112,** B08310, doi:10.1029/2006JB004712.

Laigle, M., Bécel, A., de Voogd, B., Hirn, A., Taymaz, T., Ozalaybey, S. & the Members of the SEISMARMARA Leg1, 2008. A first deep seismic survey in the Sea of Marmara: whole crust and deep basins, *Earth planet. Sci. Lett.,* **270,** 168–179.

Le Pichon, X. *et al.*, 2001. The active main Marmara fault, *Earth planet. Sci. Lett.,* **192,** 595–616.

Lévèque, J.J., Rivera, L. & Wittlinger, G., 1993. On the use of checker-board test to asses the resolution of tomographic inversion, *Geophys. J. Int.,* **115,** 313–318.

McClusky, S. *et al.*, 2000. Global positioning system constraints on the plate kinematics and dynamics in the eastern Mediterranean and Caucasus, *J. geophys.Res.,* **105,** 5695–5719.

McClusky, S., Reilinger, R., Mahmoud, S., Ben Sari, D. & Tealeb, A., 2003. GPS constraints on Africa (Nubia) and Arabia plate motion, *Geophys. J. Int.,* **155,** 126–138.

Michelini, A., 1991. Fault zone structure determined through the analysis of earthquake arrival times, *PhD thesis,* University of California, Berkeley.

Michelini, A. & McEvilly, T.V., 1991. Seismological studies at Parkfield: I. Simultaneous inversion for velocity structure and hypocenters using cubic b-splines parametrization, *Bull. seism. Soc. Am.,* **81,** 524–552.

Nalbant, S.S., Hubert, A. & King, G.C.P., 1998. Stress coupling between earthquakes in northwest Turkey and the north Aegean Sea, *J. geophys. Res.,* **103**(B10), 24 469–24 486.

Okay, A.I., Demirbag, E., Kurt, H., Okay, N. & Kuscu, I., 1999. An active deep marine strike-slip basin along the North Anatolian fault in Turkey, *Tectonics,* **18,** 129–147.

Okay, A.I., Kaslilar-Ozcan, A., Imren, C., Boztepe-Guney, A., Demirbag, E. & Kuscu, I., 2000. Active faults and evolving strike-slip basins in the Marmara Sea, northwest Turkey: a multichannel seismic reflection study, *Tectonophysics,* **321,** 189–218.

Okay, A.I., Tüysüz, O. & Kaya, Ş., 2004. From transpression to transtension: changes in morphology and structure around a bend on the North Anatolian Fault in the Marmara region, *Tectonophysics,* **391,** 259–282.

Parke, J.R., White, R.S., McKenzie, D., Minshull, T.A., Bull, J., Kuscu, I., Görür, N. & Sengör, C., 2002. Interaction between faulting and sedimentation in the Sea of Marmara, western Turkey, *J. geophys. Res.,* **107,** 2286, doi:10.1029/2001JB000450.

Pondard, N., Armijo, R., King, G.C.P., Meyer, B. & Flerit, F., 2007. Fault interactions in the Sea of Marmara pull-apart (North Anatolian Fault): earthquake clustering and propagating earthquake sequences, *Geophys. J. Int.,* **171,** 1185–1197.

Reilinger, R.E. *et al.*, 1997. Global Positioning System measurements of present-day crustal movements in the Arabia-Africa-Eurasia plate collision zone, *J. geophys. Res.,* **102,** 9983–9999.

Sato, T., Kasahara, J., Taymaz, T., Ito, M., Kamimura, A., Hayakawa, T. & Tan, O., 2004. A study of microearthquake seismicity and focal mechanisms within the Sea of Marmara (NW Turkey) using ocean-bottom seismometers (OBS), *Tectonophysics (Special Issue),* **391,** 303–314.

Sengör, A.M.C., Tüysüz, O., İmren, C., Sakınç, M., Eyidoğan, H., Görür, N., Le Pichon, X. & Rangin, C., 2005. The North Anatolian Fault: a new look, *Ann. Rev. Earth planet. Sci.,* **33,** 37–112.

Smith, A.D. *et al.*, 1995. High-resolution seismic profiling in the Sea of Marmara (northwest Turkey): Late Quaternary sedimentation and sea-level changes, *Geol. Soc. Am. Bull.,* **107,** 923–936.

Spakman, W., 1993. Iterative strategies for non-linear travel time tomography using global earthquake data, in *Seismic Tomography: Theory and Practice,* eds Iyer, H.M. & Hishahara, K., Chapman and Hall, London.

Stein, R.S., Barka, A.A. & Dieterich, J.D., 1997. Progressive failure on the North Anatolian fault since 1939 by earthquake stress triggering, *Geophys. J. Int.,* **128,** 594–604.

Straub, C., Kahle, H.G. & Schindler, C., 1997. GPS and geologic estimates of the tectonic activity in the Marmara Sea region, NW Anatolia, *J. geophys. Res,* **102,** 587–601.

Taymaz, T., 2000. Seismotectonics of the Marmara Region: source parameters of 1999 Gölcük–Sapanca–Düzce earthquakes, in *Proceedings of the NATO Advanced Research Seminar: Integration of Earth Sciences Research on the 1999 Turkish and Greek Earthquakes and Needs for Future Cooperative Research,* May 14–17, 2000, Istanbul-Turkey, pp. 26–30. Abstracts Book.

Taymaz, T., Westaway, R. & Reilinger, R., 2004. Active faulting and crustal deformation in the eastern Mediterranean region, *Tectonophysics,* **391**(1–4), 1–9.

Thurber, C., 1983. Earthquake locations and three-dimensional crustal struc-

ture in the Coyote Lake area, central California, *J. geophys. Res.,* **88,** 8226–8236.

Thurber, C., 1993. Local earthquake tomography: velocities and Vp/Vs—theory, in *Seismic Tomography: Theory and Practice,* pp. 563–583, eds Iyer, H.M. & Hirahara, K., Chapman and Hall, London.

Toksoz, M.N., Shakal, A.F. & Michael, A.J., 1979. Space-time migration of earthquakes along the North Anatolian fault zone and seismic gaps, *Pure appl. Geophys.,* **117,** 1258–1270.

Tong, C. *et al.*, 2003. Influence of enhanced melt supply on upper crustal structure at a mid-ocean ridge discontinuity: a three-dimensional seismic tomographic study of 9° N east pacific rise, *J. geophys. Res.,* **108**(B10), 2464, doi:10.1029/2002JB002163.

Um, J. & Thurber, C., 1987. A fast algorithm for two point seismic ray tracing, *Bull. seism. Soc. Am.,* **77,** 972–986.

White, R.S., Smith, L.K., Roberts, A.W., Christie, P.A.F., Kusznir, N.J. & the rest of the iSIMM Team, 2008. Lower-crustal intrusion on the North Atlantic continental margin, *Nature,* **452,** 460–464.

Wong, H.K., Ludmann, T., Ulug, A. & Görur, N., 1995. The Sea of Marmara: a plate boundary sea in an escape tectonic regime, *Tectonophysics,* **244,** 231–250.

Yaltirak, C., 2002. Tectonic evolution of the Marmara Sea and its surrounding, *Mar. Geol.,* **90,** 493–529.

Yilmaz, Y., Gokasan, E. & Erbay, A.Y., 2010. Morphotectonic development of the Marmara Region, *Tectonophysics,* **488,** 51–70.

Yolsal-Çevikbilen, S., Biryol, C.B., Beck, S., Zandt, G., Taymaz, T., Adıyaman, H.E. & Özacar, A.A., 2012. 3-D crustal structure along the North Anatolian Fault Zone in north-central Anatolia revealed by local earthquake tomography, *Geophys. J. Int.,* **188,** 819–849.

Vanacore, E.A., Taymaz, T. & Saygin, E., 2013. Moho structure of the Anatolian plate from receiver function analysis, *Geophys. J. Int.,* **193**(1), 329–337.

Wessel, P. & Smith, W.H.F., 1998. New improved version of Generic Mapping Tools released, *EOS, Trans. Am. geophys. Un.,* **79,** 579.

Zelt, C.A. & Barton, P.J., 1998. Three-dimensional seismic refraction tomography: a comparison of two methods applied to data from the Faeroe Basin, *J. geophys. Res.,* **103,** 7187–7210.

Zelt, B.C., Ellis, R.M., Zelt, C.A., Hyndman, R.D., Lowe, C., Spence, G.D. & Fisher, M.A., 2001. Three-dimensional crustal velocity structure beneath the Strait of Georgia, British Columbia, *Geophys. J. Int.,* **144,** 695–712.

Zhao, D., Hasegawa, A. & Horiuchi, S., 1992. Tomographic imaging of P and S waves velocity structure beneath northeastern Japan, *J. geophys. Res.,* **97,** 19 909–19 928.

APPENDIX: THE CHOICE OF THE CONTROL PARAMETERS

Control parameters like the maximum velocity adjustment allowed per iteration (dvpmax), the damping factor and the number of iterations have been chosen by analysing them all together.

First, several inversions of large number of iterations (20 iterations) have been run with different values of dvpmax (1, 0.5, 0.25 and 0.1 km s^{-1}). At first iterations, inversions with larger dvpmax value have produced large decreases in the data variance by increasing too much the model complexity in comparison to those with smaller dvpmax value. Since the resulting velocity model of one iteration step is used as initial model for the next iteration step, at the subsequent iterations, inversions with larger dvpmax value yield local minima, whereas the ones with smaller dvpmax value continued to fit the observed data by small changes in the model complexity. As a consequence, a maximum velocity adjustment per iteration of 0.25 km s^{-1} has been applied to the following inversions since it offers a good compromise between the convergence and the required number of iterations.

Secondly, the effect of the damping factor, which is the parameter that provides a relative weighting between the data residuals and
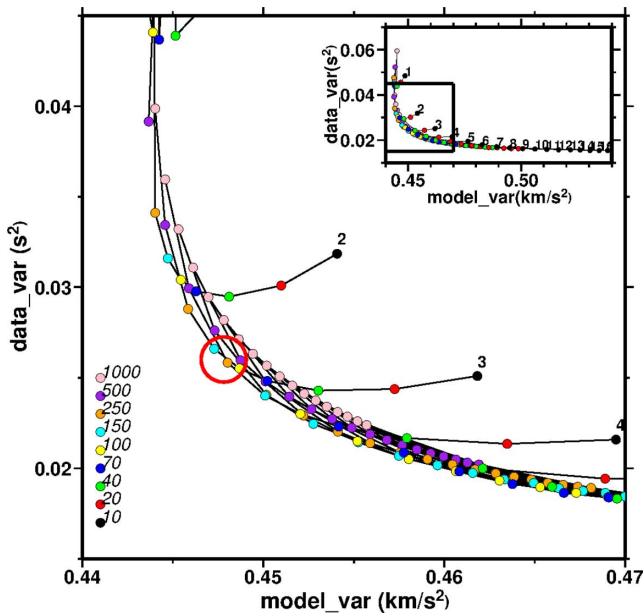
Figure A1. Zoom on the trade off curve between data and model variances of the inversion starting with the 3-D initial model. The inset shows the whole trade-off curve. Inversions with 20 consecutive iterations with damping values varying between 1000 and 10 have been run. Coloured dots represent different damping values and number of iterations are marked at the end of curves. A maximum velocity adjustment of $0.25\,\mathrm{km\,s^{-1}}$ has been applied to the inversions. Third iteration with the damping value 150 and the fourth iteration with the damping value 250 provide similar increase into the data variance, both justified by a data fit.

the model perturbation has been analysed with respect to the chosen velocity adjustment. Instead of choosing the damping value as commonly found in the literature (Eberhart-Phillips 1990), we analysed trade-off curves of the model variance versus data variance with different damping values, for 20 consecutive iterations (Fig. A1). Inversions with smaller damping values stopped before the 20th iteration with the *F*-test criterion. None of the tested damping values yield a smaller final data variance than the expected variance due to the reading error $(0.002\,\mathrm{s^2})$. The finite parametrization of the medium imposed by the size of the data set and the survey geometry is the reason why regardless to the damping value, the final data variance remain larger than the estimated variance due to the reading error. The analysis of trade-off curves has shown that, there is more than one damping value with which the increase of the model complexity is justified with a data fit. The required number of iterations depends of course on the damping values and has to be chosen accordingly (Fig. A1). In order to choose the optimum damping value and the corresponding required number of iterations, this analysis has been repeated for each tested initial model.

SUPPORTING INFORMATION

Additional Supporting Information may be found in the online version of this article:

Figure S1. (a) In red: *Vp* model beneath the OBS 10, representing the velocities of the Central Basin, in green: NMT model, in blue: basin border *Vp* model, in black: minimum 1-D model (computed by Velest), *a priori* residuals with the 3-D initial model, the basin model, the NMT model, the basin border model and the minimum 1-D model are represented in (b), (c), (d), (e) and (f), respectively. 0,

1, 2 and 3 weighted shots are shown in pink, blue, green and brown, respectively.

Figure S2. Map view of the final velocity perturbations with respect to the 3-D initial model. Blue contours surround the positive anomalies and red contours surround the negative ones. Only at the NMT borders the velocity perturbations reach up to 15 per cent. The black contour (DWS = 50) surrounds the nodes, which have been inverted during the inversion. The black crosses are the inverted nodes whereas the red ones are the fixed ones. The shots are shown in circles and the OBSs are shown in grey hexagons.

Figure S3. The comparison between the basement depth perturbations obtained by the real data inversion and by perturbing the 3-D initial model with various checkerboard patterns. The pre-kinematic and the crystalline basement depths in the 3-D initial model, approached by 4.2 and $5.2\,\mathrm{km\,s^{-1}}$ iso-velocity contours are shown in black on all cross-sections. (a) red: same iso-velocity contours in the final 3-D model (b) green: same iso-velocity contours in the model perturbed by the checkerboard pattern of $12\,\mathrm{km} \times 12\,\mathrm{km} \times 6\,\mathrm{km}$ dimensions and 5 per cent of amplitude. (b) green: same iso-velocity contours in the model perturbed by the checkerboard pattern of $12\,\mathrm{km} \times 12\,\mathrm{km} \times 6\,\mathrm{km}$ dimensions and 10 per cent of amplitude, (c) green: same iso-velocity contours in the model perturbed by the checkerboard pattern of $6\,\mathrm{km} \times 6\,\mathrm{km} \times 6\,\mathrm{km}$ dimensions and 5 per cent of amplitude. The seafloor bathymetry is represented in blue and the OBSs along the profile are in yellow circles. Notice that checkerboard models with $12\,\mathrm{km} \times 12\,\mathrm{km} \times 6\,\mathrm{km}$ dimensions represent better the real inversion topographic variations than the smaller ($6\,\mathrm{km} \times 6\,\mathrm{km} \times 6\,\mathrm{km}$) checkerboard.

Figure S4. (a) Map view of the checkerboard pattern of $12\,\mathrm{km} \times 12\,\mathrm{km} \times 6\,\mathrm{km}$ dimensions and 10 per cent of amplitude. Only 2, 4 and 6 km are perturbed with the checkerboard pattern. Other layers (0, 8 10 and 12 km) will be used to observe the eventual leakage. The black crosses are the inversion grid nodes. The shots are presented in circles and the OBSs in grey hexagons (b) synthetic inversion results, orange (RDE = 0.2) and green (RDE = 0.07) contours surrounds the good and fairly resolution areas, respectively. Notice that the threshold values of the synthetic inversion are different that real inversion threshold values. The real inversion threshold RDE values are estimated by exporting the synthetic inversion threshold RDE values over the grid-based plot of the RDE distribution. The real inversion RDE contours which best mimic the synthetic ones (good: RDE = 0.2, fairly RDE = 0.05) are chosen as the real inversion RDE thresholds. (c) Cross-section trough the model perturbed with the checkerboard pattern of $12\,\mathrm{km} \times 12\,\mathrm{km} \times 6\,\mathrm{km}$ dimensions and 10 per cent of amplitude. (d) Synthetic inversion result along the cross-section. Orange (RDE = 0.2) and green (RDE = 0.07) contours surround the good and fairly resolved areas, respectively. Blue line shows the seafloor bathymetry along the profile. OBSs are represented in yellow circles. The pre-kinematic basement topography is in black.

Figure S5. Map view of (a) the ray density (NHIT) distribution, (b) the ray crossing distribution (DWS) and (c) the diagonal element of the resolution matrix (RDE) of the final 3-D model. The contours of the threshold values of RDE (red: good resolution, RDE = 0.2 and black: fairly resolution, RDE = 0.05) are plotted on each distribution. The black crosses are inverted nodes and red ones are the fixed ones. The shots are shown in circles and the OBSs are shown in grey hexagons. White contour on (b), is the DWS = 50 contours. Nodes with DWS values smaller than 50 are not inverted.

Figure S6. (a) The ray density (NHIT), (b) the ray crossing (DWS) and (c) the diagonal element of the resolution matrix (RDE)

distributions along the profile SM36, shown in Figs 8(a) and (b). Yellow triangles represent the OBSs along this profile. The seafloor bathymetry is represented in blue. 4.2 (in green) and 5.2 km s^{-1} (in blue) contours are used as visual guides for pre-kinematic and crystalline basements, respectively. Red (RDE = 0.2) and black (RDE = 0.05 contours represent the areas with good and fairly resolution, respectively. Vertical exaggeration: 3.

Figure S7. (a) The ray density (NHIT), (b) the ray crossing (DWS) and (c) the diagonal element of the resolution matrix (RDE) distributions along the profile SM8, shown in Figs 8(c) and (d). Yellow triangles represent the OBSs along this profile. The seafloor bathymetry is represented in blue. 4.2 (in green) and 5.2 km s^{-1} (in blue) contours are used as visual guides for pre-kinematic and crystalline basements, respectively. Red (RDE = 0.2) and black (RDE = 0.05 contours represent the areas with good and fairly resolution, respectively. Vertical exaggeration: 3.

Figure S8. (a) The ray density (NHIT), (b) the ray crossing (DWS) and (c) the diagonal element of the resolution matrix (RDE) distributions along the southern E–W profile, shown in Fig. 9. Yellow triangles represent the OBSs along this profile. The seafloor bathymetry is represented in blue. 4.2 (in green) and 5.2 km s^{-1} (in blue) contours are used as visual guides for pre-kinematic and crystalline basements, respectively. Red (RDE = 0.2) and black (RDE = 0.05 contours represent the areas with good and fairly resolution, respectively. Vertical exaggeration: 3.

Figure S9. (a) The ray density (NHIT), (b) the ray crossing (DWS) and (c) the diagonal element of the resolution matrix (RDE) distributions along the N–S profile SM5, shown in Fig. 10. Yellow circles represent the OBSs along this profile. The seafloor bathymetry is represented in blue. 4.2 (in green) and 5.2 km s^{-1} (in blue) contours are used as visual guides for pre-kinematic and crystalline

basements, respectively. Red (RDE = 0.2) and black (RDE = 0.05 contours represent the areas with good and fairly resolution, respectively. The inversion nodes are shown in black crosses. Vertical exaggeration: 3.

Figure S10. (a) The ray density (NHIT), (b) the ray crossing (DWS) and (c) the diagonal element of the resolution matrix (RDE) distributions along the N–S OBS-line 3 shown in Fig. 11(a). Yellow triangles represent the OBSs along this profile. The seafloor bathymetry is represented in blue. 4.2 (in green) and 5.2 km s^{-1} (in blue) contours are used as visual guides for pre-kinematic and crystalline basements, respectively. Red (RDE = 0.2) and black (RDE = 0.05 contours represent the areas with good and fairly resolution, respectively. Vertical exaggeration: 3.

Figure S11. (a) The ray density (NHIT), (b) the ray crossing (DWS) and (c) the diagonal element of the resolution matrix (RDE) distributions along the E–W tomographic section at the latitude 40.8218° cutting across the deeper part of the basins, shown in Fig. 12. Yellow circles represent the OBSs along this profile. The seafloor bathymetry is represented in blue. 4.2 (in green) and 5.2 km s^{-1} (in blue) contours are used as visual guides for pre-kinematic and crystalline basements, respectively. Red (RDE = 0.2) and black (RDE = 0.05 contours represent the areas with good and fairly resolution, respectively. The inversion nodes are shown in black crosses. Vertical exaggeration: 3 (http://gji.oxfordjournals.org/lookup/suppl/doi:10.1093/gji/ggt211/-/DC1).

Please note: Oxford University Press is not responsible for the content or functionality of any supporting materials supplied by the authors. Any queries (other than missing material) should be directed to the corresponding author for the article.